UNIVERSITÀ DEGLI STUDI DI PAVIA

FACOLTÀ DI INGEGNERIA

DIPARTIMENTO DI ELETTRONICA

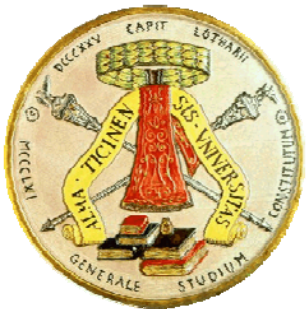

DOTTORATO DI RICERCA IN MICROELETTRONICA
XXIII CICLO

A NOISE SHAPING TECHNIQUE FOR HIGH SFDR BASEBAND FILTERS

Tutore:
Chiar.mo Prof. Rinaldo Castello

Coordinatore:
Chiar.mo Prof. Franco Maloberti

Tesi di dottorato di
Alberto Pirola

Contents

Introduction

The main goal of a wireless receiver is the detection of a low power signal among strong interferers present across the spectrum. Such an operation requires filtering out of band unwanted signals without deteriorating the desired signal present in the band of interest. This results in a very challenging spurious free dynamic range (SFDR) requirement for the channel-select filter that has to manage at the same time a small signal and high level blockers. The core of a filter design is to take advantage of the noise-power-area and linearity trade-off to achieve the best match between the filter performance and the system requirements ([1]).

The amount of noise introduced by standard filters is proportional to kT/C and is concentrated in the filter pass band, for this reason, once the noise filter floor is set, the amount of capacitance is roughly defined and, with it, a minimum in terms of area and power consumption ([2]). The presence of a lower bound in the achievable in-band noise forces to have a minimum amount of gain (to be achieved with a sufficient linearity) before the filtering. This results in an increment of the power consumption not only for the filter, but also for the preceding stage, that performs the linear amplification.

The solution presented in this thesis work aims to break these trade-offs by inserting an in-band zero in the transfer function for the input noise sources. This shapes the noise spectrum allowing to reduce the filter noise floor without increasing power consumption and capacitance. In addition to in-band noise shaping, this solution allows also to filter a large amount of the out-of-band interferers before they enter the active devices, with a benefit on the spurious free dynamic range (SFDR).

In **chapter 1** an overview of the channel selection filters state-of-the-art is presented. In particular, the most effective techniques used to increase the filters SFDR are described and deeply analyzed. Finally, a noise-shaping baseband filter solution is also described.

In **chapter 2** the fundamental trade-off of the standard filters, between in-band noise and capacitance value, is analyzed, and it is also proposed a theoretical so-

lution to overcame that limit. Then, the "pipe filter" concept is introduced and a real "pipe filter" implementation is described. In particular the "pipe filter" performances in terms of dynamic range are investigated, in order to point out its peculiar features.

In **chapter 3** a "pipe filter" biquad cell is presented and analyzed, with particular focus to its performances in terms of in-band noise and linearity. Then, a 4^{th} order channel selection filter prototype, designed for WCDMA standard, is described and all the design issues are examined. Finally, a complete set of experimental measurements carried out on the $90nm$ filter protoype are reported.

Chapter 4 deals with a current-based reconfigurable front-end for both GSM and UMTS standards. In the first section the GSM and UMTS general features are reported and all the receiver specifications are derived for both standards. Then, the front-end design is described, with particular focus on the "pipe filter" biquad cell, used as the baseband channel selection filter: the filter topology is shown and all the design issues are investigated. Finally, the front-end simulation results are reported.

Chapter 1

The Channel Selection Filters State-of-the-Art

Contents

Most of narrow-band wireless standards, like GSM, WCDMA or WLAN, shows an interferers scenario with high level blockers very close to the desired signal bandwidth. These signals cannot be filtered out at high frequencies, where an adequate selectivity is not feasible, and they can occur at the baseband filter input without any preceding attenuation. Thus, one of the main challenge in a wireless receiver design is the baseband filter capability to manage these high level blockers, without introducing a significant amount of in-band noise. It means that a very high SFDR is required.

In this chapter, an overview on the state-of-the-art of baseband channel selction filters is proposed, with particular focus on the high dynamic range solutions and on the noise reduction techniques.

1.1 Active G_m-RC Low Pass Cell

In [3] an Active-G_m-RC approach is proposed. The basic biquadratic cell presented in this work shows a closed-loop structure that exploits the opamp frequency response in the filter transfer function. This corresponds to operate with an opamp unity-gain-frequency comparable with the filter pole frequency, and, thus, to minimize the power consumption with respect to other closed-loop structures, having higher gain-bandwidth product.

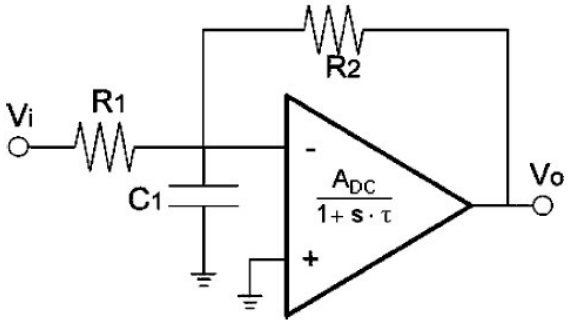

Figure 1.1: Active-G_m-RC biquadratic cell ([3])

Fig.1.1 shows the second-order low-pass Active-G_m-RC cell structure in its single-ended form.

The opamp has a single-pole transfer function (in the frequency range of interest), written as

$$A(s) = \frac{A_{DC}}{1 + s\tau} = \frac{\omega_u \, \tau}{1 + s\tau} \tag{1.1}$$

where $1/\tau$ is the opamp first pole angular frequency, ω_u is the opamp unity-gain angular frequency and A_{DC} is the opamp DC gain.

This Active-RC cell, according to [3], exhibits the following features that make it preferable for the implementation of baseband filter of portable multistandard terminals.

- **low power consumption** (key target for portable terminals): one opamp is used to synthesize a second-order transfer function, halving the power consumption compared with standard two-opamp Active-RC biquad cells. In addition, the opamp frequency response is used to synthesize the filter frequency response. Thus, the opamp unity gain bandwidth, f_u , is comparable with the filter pole, f_{LP} (f_u/f_{LP} is in order of magnitude of unity for most of designs). This reduces its power consumption with respect to a standard closed-loop structures (Active-RC or MOSFET-C), in which the

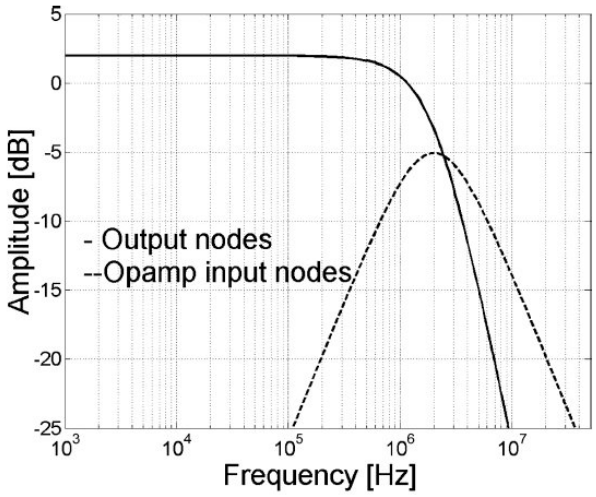

Figure 1.2: The Active-G_m-RC biquad cell frequency response to the output node and to the opamp input node. ([3])

opamp unity-gain bandwidth has to be much larger than the filter pole (typically $f_u > 50 \div 100 f_{LP}$ is used), requiring a much larger power consumption;

- **high linearity**: a very large linear range is achieved due to its closed-loop structure. Fig.1.2 shows the frequency response to the output node and to the opamp input node, where the signal is always very low, reducing the opamp in-band distortion. Moreover, out-of-band signals are firstly filtered by the absolutely linear low-pass filter at the input. This gives an out-of-band IP3 better than the in-band IP3, which is particularly interesting in telecom systems where the out-of-band linearity is crucial (and often more important than in-band linearity) due to the higher level of out-of-band blockers.

- **frequency response accuracy**: the adjusting circuit makes the opamp frequency response dependent on the passive component values (R and C) spread, which is the only spread to be compensated and this is done by a tuning system.

1.2 Anti-Blocker Structure MOSFET-C Filter

In [1] is presented a filter design technique that offers a high signal-to-blocker dynamic range performance, using a MOSFET-C filter with a prefilter. The main

goal of this approach, is to design highly linear baseband filters with accurate response.

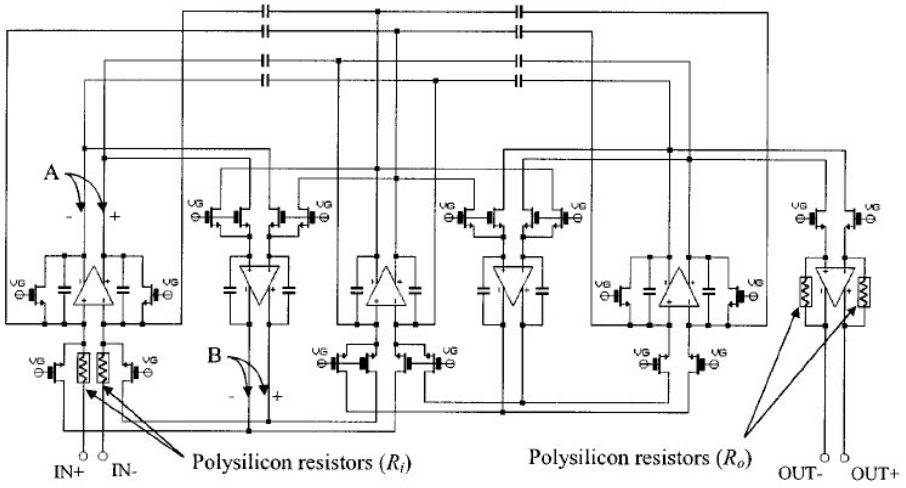

Figure 1.3: Anti-blocker structure MOSFET-C low-pass filter ([1])

In Fig.1.3, the proposed anti-blocker structure MOSFET-C low-pass filter is shown. The MOSFET-C low-pass filter employs a leapfrog structure that realizes transmission zeros [4]. In a classical MOSFET-C structure, the resistors of an active RC filter are replaced by MOSFETs, and all MOSFET pairs are operated in balanced fashion in the triode region. This cancels the even-order distortion of MOSFETs, which is the dominant nonlinearity in this case. The gate voltage of the MOSFETs (V_G) can be automatically tuned to make the frequency response stable. The MOSFET-C approach has also a potential advantage in comparison to the $G_m - C$ approach. In $G_m - C$ filters, each transconductor consists of several devices, each of which contributes to excess noise. In contrast, each triode-operated MOSFET in Fig. 1.3 contributes noise practically equal to that of an equivalent resistor, and the op amps can be designed so that their noise contribution is below that of the filter resistors. Thus, assuming both types of filters are well-designed, lower noise (often by a factor of 3 or more) can be obtained with the MOSFET-C approach, assuming the same total capacitance. To be able to take advantage of this to achieve a correspondingly higher dynamic range, though, one must make sure that the triode-operated MOSFETs can handle large signal swings with sufficiently small distortion.

In order to improve the out-of-band linearity of the filter, a pair of polysilicon resistors (R_i) is used in the input part of the filter [shown by heavy lines in Fig. 1.3. This accomplishes highly linear voltage-to-current conversion thanks

to the virtual short property of the input node of the operational amplifier. In such an implementation, the lack of tracking between R_i and other MOSFET resistors cause only a variation of the filter gain; this variation is easily cancelled by adding an additional gain-compensating stage as the last stage in the filter using polysilicon resistors (R_o) as shown in Fig. 1.3. The filter gain now becomes $R_o/(2R_i)$ before dynamic range optimization, assuming all MOSFET resistances are equal. The cut-off frequency of the filter can thus be tuned using the gate voltage of the MOSFET resistors (V_g) without affecting the gain.

1.3 Channel-Select Filter With Blocker Detection

In [5] a solution for the problem of large power dissipation of channel-select filters is proposed. The main reason for this power dissipation is that they have to be designed with high linearity, for the eventuality that large blockers hit the system. However, this large power dissipation is unnecessary when such blockers are absent or are of reduced strength, which is often the case. On the contary, conventional channel-select filters are designed for the case of small in-band signal and high level out-of-band blockers, and are thus being operated with an excessive available dynamic range for a significant fraction of their operation time, when the above worst case situation does not occur. Thus it can be desirable that the receiver effectively measure the blocker levels, and that the system be designed to be able to handle such large blockers, but not to waste the large current such handling requires when such blockers are not present.

In Fig. 1.4, the concept of the level detector implemented with a first-order opamp-RC filter is presented. In this system, the level detector uses the opamp input voltage V_x as the input signal, and feeds back the control signal to modify the opamp gain magnitude $|A(f)|$ with respect to the blocker levels at out-of-channel frequencies. In the control loop shown, the level detector circuit compares the envelope of V_x with a reference voltage, and feeds a bias control signal V_{CNT} back to the opamp, thus adjusting the open-loop gain of the opamp, $|A(f)|$, by controlling its transconductance.

1.4 Multiple-G_m Reconfigurable Low Pass Filter

In [6] a low-pass filter with continuous tuning over a very wide range suitable to be used in a zero-IF receiver is provided. This can be useful because a large continuous tuning range is aimed at covering bandwidth requirements of the various communication standards in use today, and recent demand for multistandard

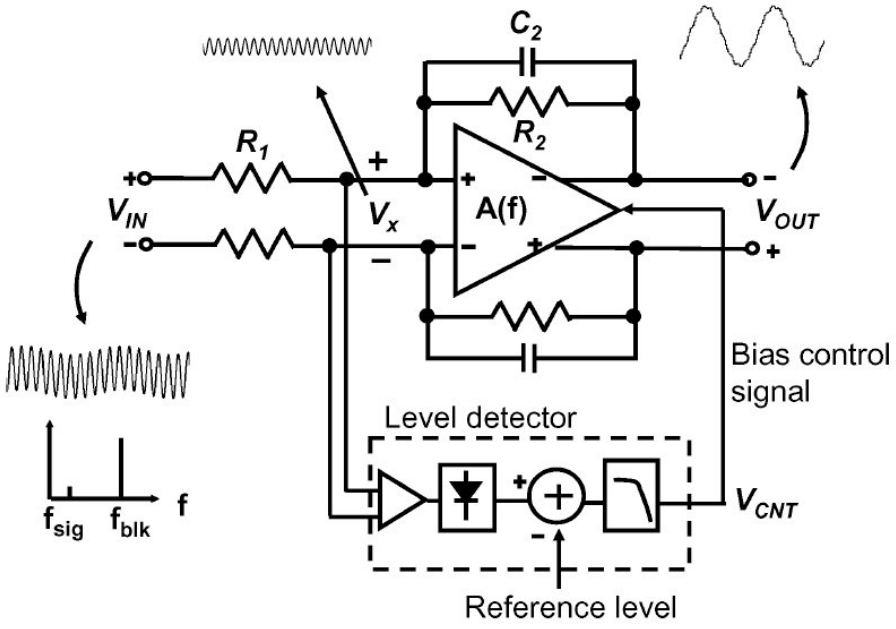

Figure 1.4: First-order opamp-RC filter implemented with a bias control loop. ([5])

transceivers has been leading to frequent use of direct conversion architectures, notably because of their high integration potential and their relative system design easiness.

This work ([6]) presents a $G_m - C$ implementation of an LC ladder filter, chosen mainly because it provides low sensitivity to process variations, temperature drifts, and aging when associated with an on-chip automatic tuning system. Moreover, G_m-tuning allows a perfectly continuous tuning over a wide frequency range. To extend the tuning range beyond the transconductor's intrinsic tuning range, G_m-switching or capacitor-switching could be implemented. G_m-switching presents some important advantages compared to capacitor-switching. Indeed, with G_m-switching the maximum capacitance value is always used, thus maximizing the signal-to-noise ratio. Moreover, no switch has to be implemented on the signal path, so any issue relative to series resistance or switch linearity is avoided. Moreover, a G_m-switching topology keeps the parasitic capacitance constant on the signal nodes, making the layout implementation straightforward.

In [6], third-order Butterworth filter transfer function is implemented using an LC ladder network. If no capacitor switching is being used, the simple structure's tuning ratio would be equal to that of a single transconductor and hence would have to be around 30. Unfortunately, one single transconductor can hardly provide this tuning range with satisfactory performances, especially in terms of linearity,

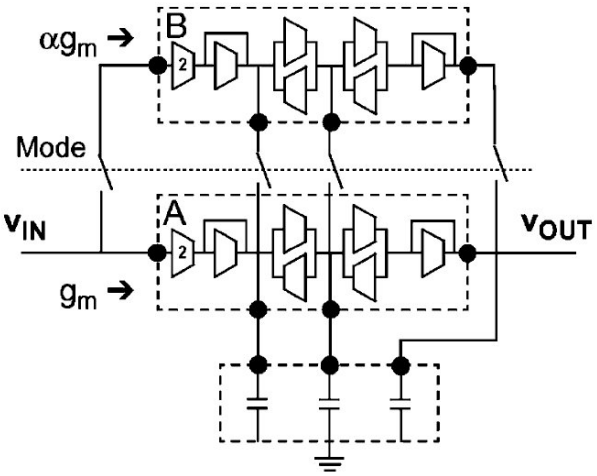

Figure 1.5: Multiple-G_m reconfigurable low-pass filter structure. ([6])

noise, or power consumption.

Thus a multiple-G_m configuration structure (see Fig. 1.5), allowing a significant increase in the f_{max}/f_{min} ratio, is proposed. In this case, two transconductor banks are connected in parallel to one single integration capacitor bank, so that the effective transconductance value is the sum of each of the transconductance cells. Within one transconductor bank, all of the transconductors present the same g_m value.

1.5 Switchable-Order G_m-C Baseband Filter With Wide Digital Tuning

In [7] the design of a widely-tunable, topology-configurable $G_m - C$ filter complying to a large number of standards is presented. This filter can also optimize the usual resources in the semiconductor industry i.e., area and power consumption. In fact, reconfiguration of the filter order adds an additional degree of freedom to optimize power consumption and dynamic range. Because of its simplicity, an LC-ladder $G_m - C$ implementation has been chosen over a biquad scheme. Moreover, such structures usually provide also improved sensitivity properties.

$G_m - C$ ladder topologies consist of input/output terminals and a chain of gyrators loaded by capacitors [8]. Apart from the I/O terminals, such a topology can be regarded as a series of basic structures consisting of two transconductors forming a gyrator, around which two grounded capacitors are connected, as depicted in Fig. 1.6 and henceforth it can be considered as the "basic cell" for this

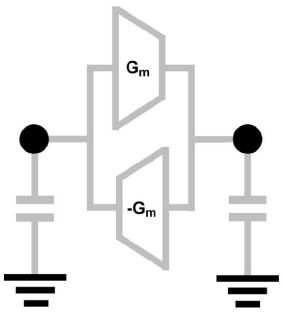

Figure 1.6: Basic cell consisting of two grounded capacitors connected to a pair of transconductors. ([7])

topology. In order to build the topology-configurable pattern, the highest-order structure is broken down into elementary basic cells, and some of these can be by-passed and turned off, allowing a reduction of power consumption for lower-order configurations.

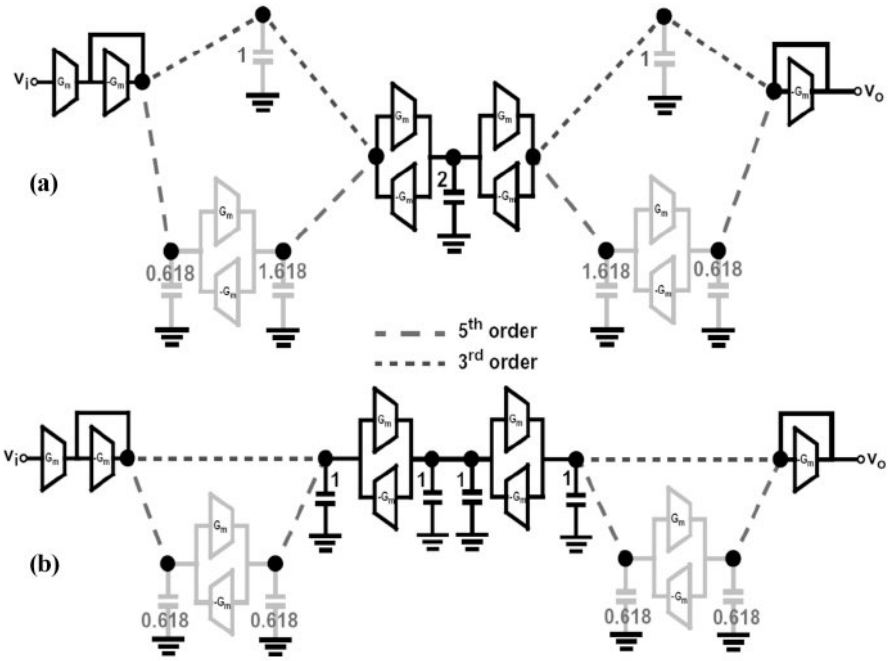

Figure 1.7: Third/fifth-order switchable Butterworth $G_m - C$ low-pass filter. (a) Basic configuration. (b) Optimized implementation. ([7])

Fig. 1.7(a) shows an example of third/fifth-order switchable Butterworth $G_m - C$ low-pass filter, starting from the basic configuration, using the cell reported in Fig. 1.6. Sharing as much as possible capacitors between the third-order and fifth-

order topologies leads to the implementation shown in Fig. 1.7(b). This technique here allows a 25% saving on capacitor area and power consumption and achieves a perfect symmetry in each of the basic cells. Although this technique is extendable to any topology, the third/fifth-order Butterworth configurability offers the best results in terms of area savings and symmetry.

1.6 Source Follower Based Filter

In [9], a further alternative is proposed, based on a complex source-follower topology. It is well known that the source-follower structure uses an internal feedback loop that increases linear range while reducing input MOS overdrive voltage. This feature is exactly the opposite of any reported filtering technique, which requires large overdrive for large linearity. This, as a consequence, would increase the current (and power) level for a given transconductance to be performed. On the contrary, the proposed structure improves linearity while reducing overdrive and the current level, and, as a consequence, the power consumption.

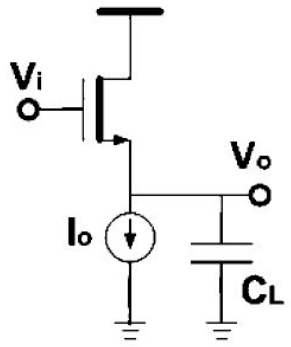

Figure 1.8: Source-Follower. ([9])

The source-follower, shown in Fig. 1.8, is the basic kernel of the proposed second-order cell. The source-follower, largely used in the signal processing, presents some interesting features that make it very attractive to design analog filters. First, it has a good linearity, due to the presence of the local feedback. As any feedback structure, its linearity improves with a large closed-loop gain, which for the source-follower is given by $G_{loop} = g_m/(g_{ds} + g_{do})$, where g_{do} is the I_0 current source output conductance. This means that a larger transconductance (g_m) value results in a larger loop gain and then in a better linearity. This basic conclusion completely differs from other active filters (like $g_m - C$ filters, for instance), where the linearity is improved at the cost of larger V_{OV}, and then

larger current (for a given g_m) and power consumption. Breaking the dependence V_{OV}-versus-linearity immediately has a large impact on the power performance.

Moreover, a time constant C_L/g_m is obtained depending only on the transistors transconductance and on the capacitive load. This means that the circuit does not need to drive any resistive load, avoiding having to consume current under signal regime.

Furthermore, the cell presents more advantages that allow reduction of the current consumption requirement. For example, no circuital parasitic poles are present. In fact, each circuit node correspond to a pole included in the cell transfer function. Therefore, there is no need of extra current to push parasitic poles to higher frequencies.

In addition, the source-follower can drive a resistive load without substantially modifying its linearity performance and its pole frequency.

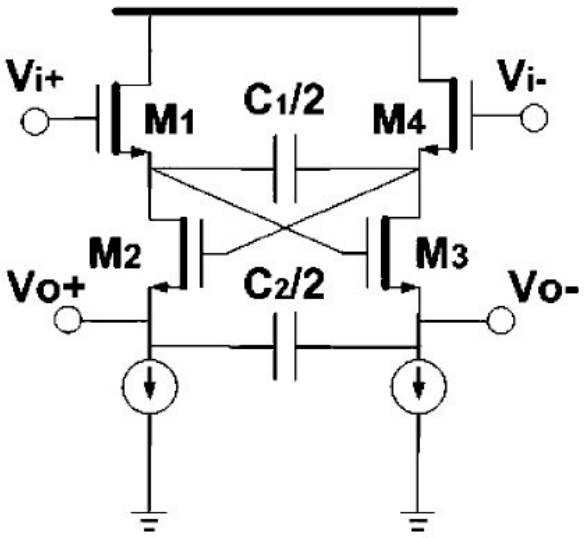

Figure 1.9: Source-Follower-Based Biquad Cell. ([9])

The advantages of the source-follower above described are exploited in the second-order low-pass cell shown schematically in Fig. 1.9.

This cell presents an optimized single-branch fully differential structure and operates like a "composite" source-follower. In fact, it performs an ideal unitary DC-gain. All the transistors are designed with the same sizes and draw the same current levels. As a consequence, they all exhibit the same tranconductance, which can be written as

$$g_{m1} = g_{m4} = g_{m2} = g_{m3} = g_m \tag{1.2}$$

The key proposal of this cell is the positive feedback in MOS devices and , which allow synthesis of two complex poles. Assuming that the transistorÕs output conductance is much smaller than the transconductance, the filter transfer function is

$$H(s)) - \frac{1}{s^2 \frac{C1 \cdot C2}{g_m^2} + s\frac{C1}{g_m} + 1} \tag{1.3}$$

The filter par

1.7 Dual Mode Baseband Filter

In [10], a dual-mode baseband filter for WCDMA and PDC systems was designed. These systems represent the two extremes with respect to channel bandwith, which makes combining them difficult.

In WCDMA mode, a fifth-order Butterworth filter with a cutoff frequency of 2.1 MHz was found to fulfill the system selectivity requirements. The wide bandwidth in WCDMA mode leads easily to high power consumption. Therefore, full channel selection filtering was implemented in analog domain to relax the ADC requirements and to eliminate power-consuming highspeed digital filtering.

In PDC mode, it was assumed that a larger ADC resolution is easily obtainable and the filter order was reduced to three, the cutoff frequency being $13kHz$. The low corner frequency of the PDC filter leads to large passive components occupying a lot of die area. The differential integrators in the PDC filter required a chip area of up to $0.4mm^2$, whereas a 16-bit digital integrator in the same process requires only $0.00816mm^2$. Consequently, the total area was reduced by transferring some of the channel filtering to digital side. One stopband zero was added to the third-order Butterworth prototype as this was found to relax the ADC performance requirements and the roll-off requirements of the subsequent digital filter.

A leapfrog circuit architecture was chosen over cascaded biquads because of the well-known low sensitivity. Furthermore, the realization of the stopband zero is very straightforward in this case (Fig. 1.10). The opamp-RC technique was chosen over the switched capacitor (SC) technique since an SC filter would have required a continuous-time prefilter, which was clearly undesirable. Furthermore, the chosen process features high ohmic resistors and the chip area was found to be determined mostly by the capacitors.

As the fifth-order WCDMA-mode filter requires two operational amplifiers more than the PDC-mode third-order filter, two operational amplifiers are disconnected from the filter and powered down in PDC mode. Opamps at the both

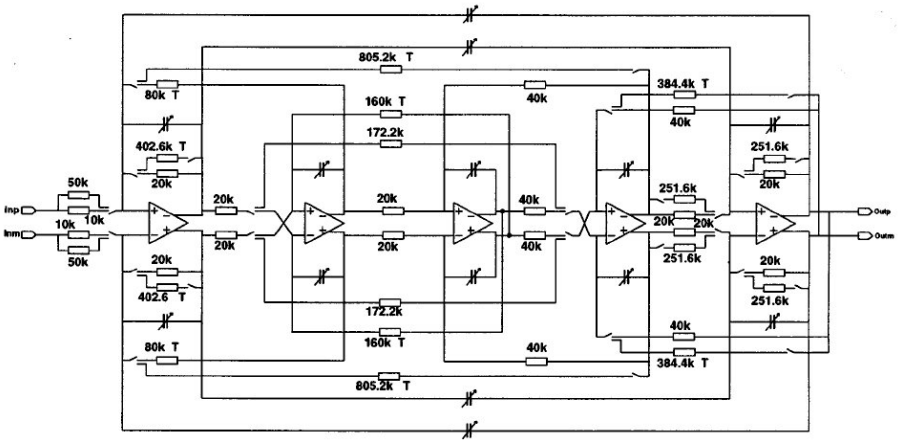

Figure 1.10: Simplified schematic of one channel. Letter T next to a resistance value denotes T network realization. ([10])

ends of the filters have connections to termination resistances and to transfer function zero capacitors, so it is logical that they are shared between the two modes. The second and third opamp were chosen to be disconnected from the filter in the PDC mode.

A gain of 18 dB was implemented in the filter to optimize its dynamic range and an additional 12 dB in an output buffer to further suppress the effect of the ADCÕs noise on the overall noise figure. Regarding noise, the placement of gain is straightforward. Placing all the gain to the first possible stage suppresses all noise sources after it when referred to the input. In the WCDMA mode, the impedance level has to be low because the channel bandwith contributing to noise is wide. Unfortunately, decreasing the impedance level requires high drive capability from the opamps which leads either to large power consumption or distortion. As the first opamp dominates the stopband distortion, its bias current was made two times larger than the current in other opamps. This had the effect of roughly halving the distortion. The gain was divided so that the intermodulation distortion from the IIP3 test was in the same order as the output noise.

1.8 A current Mode FIlter for Software Radio Applications

In [11] a current-mode low-pass filter for a transmitter for software-radio application is presented. The main advantage of such solution is that the current-mode filter needs less supply current than the I/V converter, voltage-mode filter and V/I

converter. This filter is designed to be put immediatly after a DAC based on a current-steering architecture, and before a current-mode mixer. All these current-mode blocks together can be considered as a current-mode architecture.

The first stage of the filter presented is based on an approach which consists of current mirrors and integration capacitors. In the second stage of the filter, an opamp filter, the voltage of the opamp-output is transformed into a current.

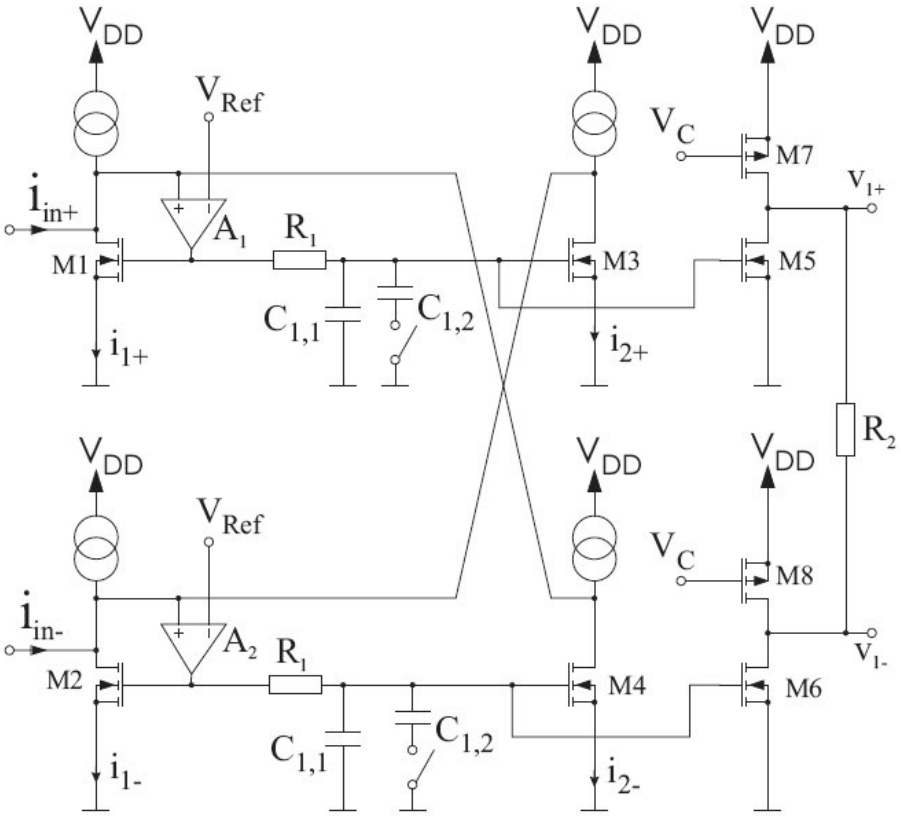

Figure 1.11: Input Filter ([11])

The cross connection of two dual current mirrors with a capacitor forms a fully balanced 1^{st}-order current-mode low-pass (see Fig. 1.11). This cross interconnection between the current mirrors provides a high differential gain and a low common-mode gain. This current-mode low-pass is now extended by the resistor $R1$. The transfer function of this filter here is given by:

$$H(s) = \frac{i_{2+}}{i_{in+}} = \frac{i_{2-}}{i_{in-}} = \frac{\frac{\alpha}{1-\alpha}}{1 + s \cdot (R_1 + \frac{1}{g_{m1}}) \cdot C_1 \cdot \frac{1}{1-\alpha}} \tag{1.4}$$

The $3dB$ cut-off frequency can be calculated as

$$f_C = \frac{1}{2\pi \cdot (R_1 + \frac{1}{g_{m1}}) \cdot \frac{1}{1-\alpha} \cdot C_1} \tag{1.5}$$

where α denotes the g_m ratio between the transistiors M3 and M1 as well as M4 and M2, respectively. ($\alpha = \frac{g_{m3}}{g_{m1}} = \frac{g_{m4}}{g_{m2}}$). The filter is designed to be switchable between two cut-off frequencies. In order not to increase the noise level by a larger resistor, the value of the capacitance is changed.

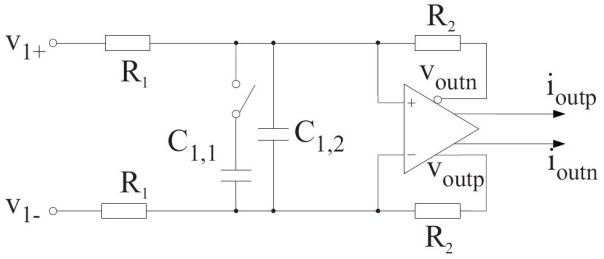

Figure 1.12: 2nd-order Filter ([11])

The 2^{nd}-stage consists of an active RC-voltage-mode filter (see Fig. 1.12). In this filter design the capacitor C_1 and the compensation capacitors define the poles.

The transfer function with the filter parameters are given by:

$$H(s) = \frac{A{\omega_0}^2}{s^2 + \omega_0/Q \cdot s + {\omega_0}^2} \tag{1.6}$$

with

$$A = \frac{R_2}{R_1} \tag{1.7}$$

$$Q = \frac{1}{A+1}\sqrt{\frac{G_{m,in}R_2C_1}{C_C}} \tag{1.8}$$

$$\omega_0 = \sqrt{\frac{G_{m,in}}{R_2C_1C_C}} \tag{1.9}$$

where $G_{m,in}$ is the resulting input transconductance which is $1/(R_S + 1/g_{m,1})$. The resistor R_C eliminates the zero in the right-half complex plane which is given by the Miller compensation. Two more transistors (M9, M10) are connected to the output which convert the voltage into the current due to the fact that the gate source voltage of the transistors M5 and M9 as well as M6 and M10 are equal. The low-pass consisting of R_{out} and C_{out} gives some additional attenuation at higher frequencies.

1.9 Active Filters with Passband Noise Shaping

The solution presented in [12] aims to break the rade-offs of the clasical base-band filter topologies for radio receivers, in terms of noise, area and power con-

sumption.

The solution proposed is a FDNR (Frequency Dependent Negative Resistance) based filtering technique, which offers several advantages in terms of noise with its noise shaping characteristics. Employing this technique in the receive chain of a radio can enhance the overall performance of the radio, an improvement that can not be achieved using classical gain-filtering techniques unless area and power consumption are sacrificed.

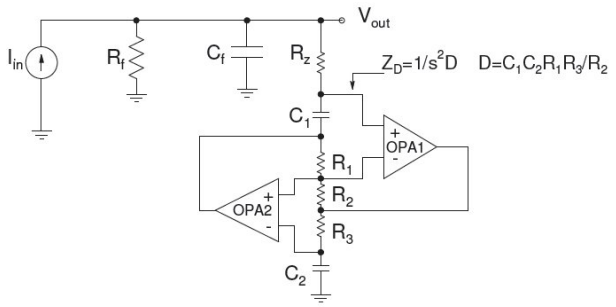

Figure 1.13: Schematic of the proposed third-order elliptic circuit. ([12])

The main advantage of the third order configuration of Fig. 1.13 is that it uses only one resistor in the signal path, the load resistor of the proceeding stage R_f, to realize the desired filter transfer function. Hence the load resistance of a mixer or of a gm stage can be reused as a part of the filter transfer function which is not the case for classical filter topologies. The noise contribution of this particular resistor is already accounted for in the preceding mixer stage. The additional noise of the FDNR resistors R_1, R_2, R_3, is shaped. Since the opamps are not in the signal path neither, their noise contributions are also shaped and hence have less contribution to the overall filter noise. Moreover, as opposed to classic filter topologies, the opamps of the proposed third-order section are not in the signal path and hence do not contribute any IQ mismatch or DC offset, which is a much desired property in a receiver chain. The signal transfer function of this circuit from input to output can be written down as follows:

$$\frac{V_{out}(s)}{I_{in}(s)} = \frac{R_f(s^2 DR_z + 1)}{s^3 DR_z R_f C_f + s^2(DR_z + DR_f) + s(R_f C_f) + 1} \tag{1.10}$$

$$D = \frac{C_1 C_2 R_1 R_3}{R_2} \tag{1.11}$$

This signal transfer function provides a notch at a frequency, $\omega_{notch} = \frac{1}{\sqrt{DR_z}}$, and the notch frequency depends on the value of D and R_z.

The schematic including the noise sources in an FDNR is shown in Fig. 1.14. In

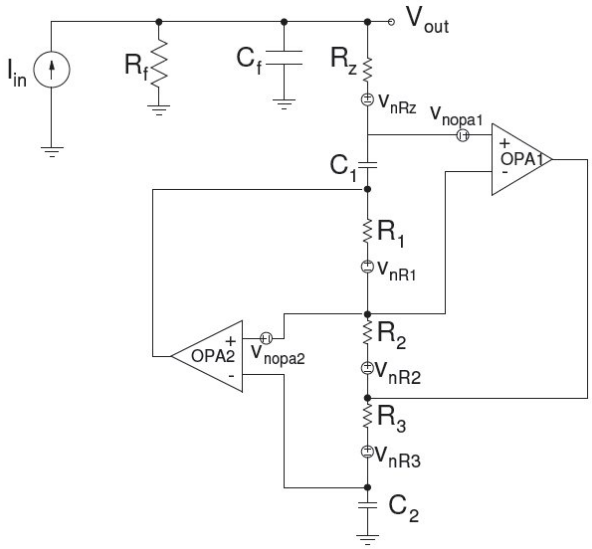

Figure 1.14: Schematic including the noise sources in the circuit. ([12])

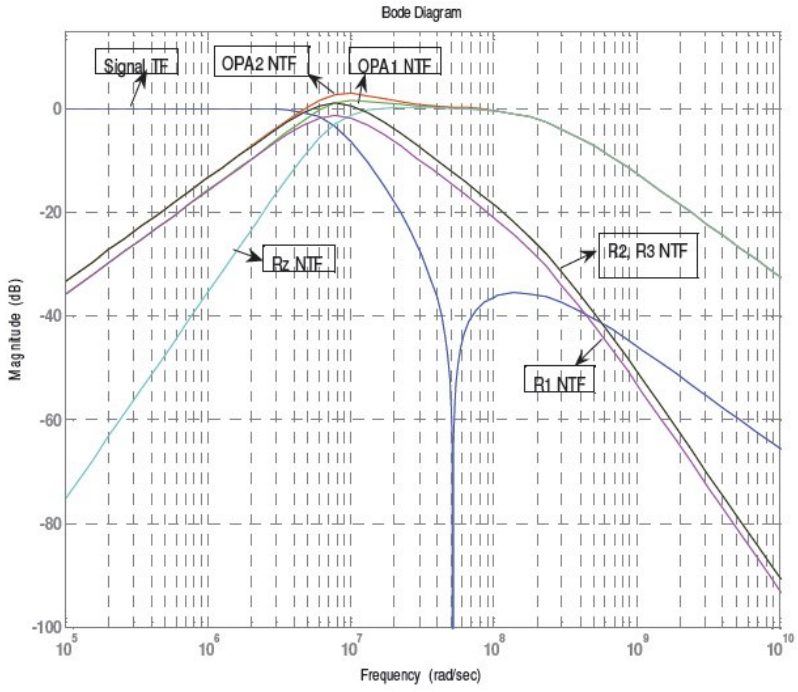

Figure 1.15: Signal and noise transfer functions of the proposed circuit. ([12])

the proposed circuit, the noise of all passive and active components in the FDNR section, namely of R_z, R_1, R_2, R_3, *OPA1* and *OPA2*, is shaped, hence the only substantial noise contributor is R_f whose noise contribution is accounted for in

the amplifier or mixer noise budget.

Fig. 1.15 shows the plots for the magnitude of these noise transfer functions as well as the signal transfer function. Since the noise generated by the FDNR resistors is shaped, the designer can use larger resistors (noisier) and hence can reduce the capacitor size. This results in a significant area saving.

1.10 Conclusions

In these last years the research work about channel selection filters design has concerned particularly two main goals: the spurious free dynamic range increase and the filter reconfigurability.

This thesis work aims to take a significant contribution for the baseband filter dynamic range maximization, by introducing a novel class of filters, called "pipe filters", that will be presented in chapter 2. These filters, such as the filter described in section 1.9, exploit a noise shaping technique in order to reduce the in-band noise and to enlarge the dynamic range. This concept of noise shaping was introduced for the first time in 2008 by Tekin et al. ([12]), where a Frequency Dependent Negative Resistance (FDNR) based active RC low-pass filter implementing such a behavior was presented. However at that time no experimental verification to prove its practical viability was provided. The first integrated prototype implementing a noise shaping filter that includes also a complete set of experimental measurements on both its noise and linearity was reported in [13] and it will be presented in chapter 3.

Chapter 2

Current Filters

Contents

The high SFDR requirement for a baseband filter results in a trade-off between the in-band noise and the linearity demanded to handle close out-of-band interferers. Since the in-band integrated noise is generally proportional to $\frac{kT}{C}$, in a classical filter once the noise floor for the filter is set, the amount of capacitance is roughly defined and with it a lower bound for area and power consumption.

In this chapter the $\frac{kT}{C}$ "limit" of classical low pass filter is analyzed, and a solution that aims to break the trade off between in-band noise and capacitance value is presented. The core of the idea is the insertion of an in-band zero in the output noise transfer function and the consequential improvement of the dynamic range. The "pipe filter" concept is then introduced and a real "pipe filter" implementation is discussed, with particular focus on the analysis of its noise and linearity behavior.

2.1 Voltage Filters: the $\frac{kT}{C}$ "limit"

Usually, when analyzing classical topologies of low pass filters, the $\frac{kT}{C}$ limit is considered as a fundamental limit for the output noise [2]. This limit can be easily shown for a 1^{st} order RC passive filter (Fig. 2.1). Considering the resistance R

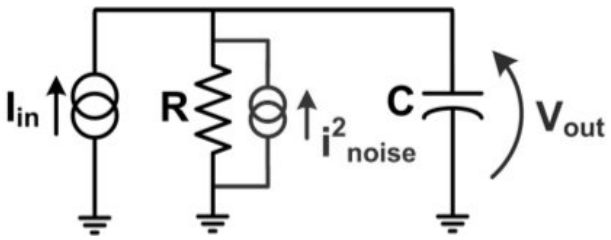

Figure 2.1: 1^{st} order RC filter

as the only noise source modeled by the noise current generator i^2_{noise}, the total noise at the voltage output V_{out} can be computed as:

$$\left\langle V^2_{noise,out} \right\rangle = \int_0^{+\infty} i^2_{noise} \cdot |Z(j\omega)|^2 = 4kTR \int_0^{+\infty} \left| \frac{1}{1 + j2\pi fRC} \right|^2 df = \frac{kT}{C} \tag{2.1}$$

The (2.1) states that the total output integrated noise is set only by the capacitance value C. It follows that, in a real filter design, the occupied area is lower limited by the noise specification, because, for a given noise target, there is a minimum capacitance value that allows to achieve it.

Another important feature of this limit, is the frequency behavior of the output noise. The spectral density, computed at the voltage output, is equal to:

$$|V_{noise,out}(\omega)| = \frac{4kTR}{1 + (\omega RC)^2} \tag{2.2}$$

This spectral density has a low pass frequency behavior at the filter output: it means that the output noise follows the same frequency behavior of the signal.

The importance of this limit is so critical, that it is worthy to be further investigated. In particular, the limit could also be quantitatively proved starting from the energy equipartition theorem ([14]). The theorem states that in a 1^{st} order low pass filter the total thermal noise energy is equal to

$$E_{noise} = \frac{1}{2}kT \tag{2.3}$$

Then, since all that noise energy is stored in the capacitor, it is also equal to:

$$E_C = \frac{1}{2}C \left\langle V^2_{noise,out} \right\rangle \tag{2.4}$$

From (2.3) and (2.4), it follows that the root mean square of the noise voltage output is equal to:

$$\left\langle V^2_{noise,out} \right\rangle = \frac{kT}{C} \tag{2.5}$$

Therefore one of the main reasons of the $\frac{kT}{C}$ limit in a low pass filter is actually the output voltage sensing across the capacitor, because all the noise energy is

actually stored in the capacitor itself. Furthermore, the capacitor is an integrator for the noise charge, hence the output noise transfer function (shown in Fig.2.2) has a low pass profile, and almost all the noise is located at low frequencies. This

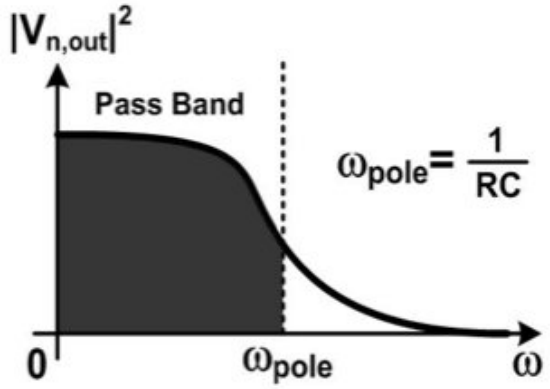

Figure 2.2: Output Noise Transfert Function in a 1^{st} order RC Filter

is a significant disadvantage for the filter signal-to-noise ratio (SNR), because the output noise is high just in the filter band, where the signal has to be read, and it becomes lower out-of-band, where the SNR has no interest.

For these reason, to overcome the $\frac{kT}{C}$ limit in a low pass filter, the output signal should not be sensed as voltage across the capacitor.

2.2 Voltage vs Current

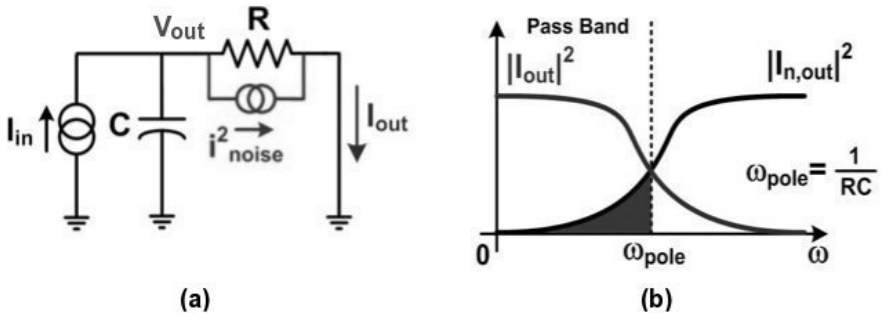

Figure 2.3: 1^{st} Order LP Filter with Current Output

In the current driven RC filter reported in Fig.2.3 there are two different way to take the output: the first is to sense the signal as a voltage across the capacitor (V_{out}), while the second is to detect the current flowing out the resistor (I_{out}). Although in both cases the input-output transfer function is a first order low pass

filter (with a single real pole located at $\omega_p = \frac{1}{RC}$), the output noise transfer function is different. In the case of a voltage output, the noise introduced by the resistor is filtered according to the signal transfer function, while in the current mode approach, the noise transfer function has a zero at DC frequency, leading to an high pass shaping (Fig.2.3.b). The difference between the two approaches is a significant in-band noise reduction in favor of the current mode one. In particular, the output noise integrated from DC to the filter cut-off frequency ω_P for the two different cases is

$$v_{noise}^2 = \frac{kT}{2C} = 0.5kT\omega_p R \tag{2.6}$$

$$i_{noise}^2 = 0.14kT\omega_p^2 C = 0.14\frac{kT\omega_p}{R} \tag{2.7}$$

where k is the Boltzmann's constant, T is the temperature, v_{noise}^2 is the voltage noise power across the capacitance and i_{noise}^2 is the current noise power flowing out of the resistor.

In terms of signal to noise ratio (SNR), a comparison can be done assuming the same in-band input signal, i.e. an input current power equal to i_{in}^2. This corresponds to an output voltage power $v_{out}^2 = i_{in}^2 \cdot R^2$ and an output current power $i_{out}^2 = i_{in}^2$. From (2.6) and (2.7), the SNR for the two configurations becomes:

$$SNR_{voltage} = \frac{v_{out}^2}{v_{noise}^2} = \frac{i_{in}^2 R}{0.5kT\omega_p} \tag{2.8}$$

$$SNR_{current} = \frac{i_{out}^2}{i_{noise}^2} = \frac{i_{in}^2 R}{0.14kT\omega_p} \tag{2.9}$$

This corresponds to $5.6dB$ better signal-to-noise ratio in favor of the current mode one.

This facts lead to a very important conclusion: a current filter can have the same in-band noise than a voltage filter with 4 times less capacitance area.

2.3 The "Pipe Filter" Concept

An interesting way to describe this low pass current filter is to consider it as a "pipe-line" ([15]) in which current is flowing and where a signal attenuation (frequency dependent) corresponds to a current loss through a leakage. Under this model, in the pass band, the filter works as a lossless pipe where the input current is equal to the output one and thus no noise or distortion can be added to it (Fig.2.4.a). On the contrary, in the stop band, any current leakage allows both noise and distortion component to enter the pipe and reach the output. This

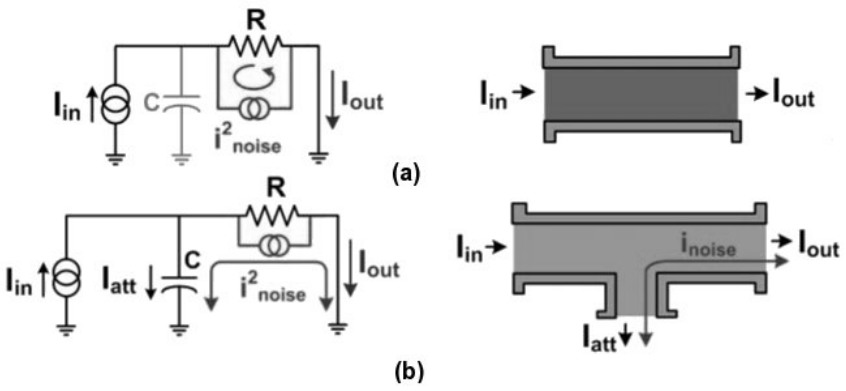

Figure 2.4: "Pipe Filters"

occurs for example for the noise produced by the transistor when the capacitor is no more an open circuit (Fig.2.4.b). As the current leakage, also the current injection required to provide an amplification can introduce noise, such as any kind of operation performed on the current that flows in the pipe. For this reason to ensure (at least ideally) that no noise is introduced in the pass band, such kind of filter must have a unitary input to output transfer function.

2.4 "Pipe Filter" Implementation

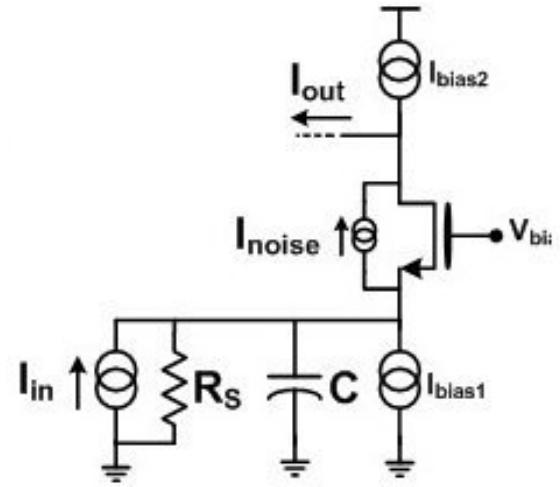

Figure 2.5: 1^{st} Order "Pipe Filter" Implementation

The current driven $g_m - C$ circuit shown in Fig.2.5 ([15]), implements a first order low pass (LP) filter (with a single real pole located at $\omega_p = \frac{g_m}{C}$, assuming

$g_m \gg \frac{1}{R_S}$). The key feature of this filter is the fact of producing a high pass shaped output current noise spectrum $|I_{n,out}|^2$ due to the presence of an in band zero in the transfer function from the transistor noise source to the output (as in Fig.2.3.b). This behavior can be explained considering that, at very low frequencies, capacitance C is a high impedance, which forces the noise to re-circulate inside the transistor. On the contrary, at high frequencies, when the capacitance becomes a low impedance, all the current noise can flow to the output. More generally, the impedance associated with input current source creates an in-band degeneration for the transistor that minimizes noise and increases linearity, as it will be seen later.

2.4.1 High Pass Noise Shaping

The noise spectral density produced by the transistor at the filter output is equal to

$$Noise_{out}(\omega) \simeq 4\ k\ T\ \gamma\ g_m \left| \frac{j\frac{\omega}{\omega_p} + \frac{1}{g_m R_S}}{1 + j\frac{\omega}{\omega_p}} \right|^2 \tag{2.10}$$

where γ is the gamma coefficient of the FET thermal noise model. As expected, this expression displays a high pass shape. However, due to the finite driving impedance R_S, the zero in the noise transfer function is no located at DC but it is moved at $\frac{\omega_p}{g_m R_S}$).

The effect of the finite driver impedance is the introduction of an additional in-band loss that lets some extra noise to come out also in the pass band. To better understand the impact of the zero on the total filter output noise, equation (2.10) can be rewritten as

$$Noise_{out}(\omega) \simeq 4\ k\ T\ \gamma\ g_m\ \frac{(\frac{\omega}{\omega_p})^2}{1 + \frac{\omega}{\omega_p}} + \frac{4\ k\ T\ \gamma}{g_m {R_S}^2} \cdot \frac{1}{1 + \frac{\omega}{\omega_p}} \tag{2.11}$$

where the total output noise is given by the sum of two terms: one still proportional to gm and high pass shaped, plus one inversely proportional to gm which does not take any advantages from the zero introduced. The presence of a terms inversely proportional to gm sets a lower bound on the transconductance that can be used to synthesized the filter for a given total integrated output noise. In particular, integrating 2.11 in the filter pass band (i.e. from 0 to ω_p) the second terms exceeds the first one for $g_m < \frac{2}{R_S}$. In Section 2.2 it is shown that for the ideal case in which the zero is located at DC, this approach increases the in band signal-to-noise ratio (SNR) by at least $5.6dB$ compared to a classic ^{1st} order LP filter without noise shaping.

2.4.2 Intermodulation Distortion Mechanisms

Due to the same reason that produces an in-band noise shaping, no intermodulation product (IM) can be generated in the filter pass band as long as the output current is equal to the input one (lossless-pipe). Notice that this is valid independently of the location of the interferers with respect to the filter pass band. This mechanism can be verified evaluating the in-band third order intermodulation product (IM3) generated at ω_{IM3} (with ω_{IM3} located in the pass band) by two tones located out of the filter pass band at ω_1 and at $2\omega_1 - \omega_{IM3}$. Using Volterra's series approach ([16], [17]) and assuming for the transistor characteristic a Taylor expansion with g_i as the i^{th} order coefficients, the power of the intermodulation term $|IM3(\omega_{IM3})|^2$ is given by

$$|I_{IM3}(\omega_{IM3})|^2 \simeq \left| j\frac{\omega_{IM3}}{\omega_p} + \frac{1}{g_m R_S} \right|^2 |X(\omega_1, \omega_p)|^2 \, {I_1}^2 I_2 \tag{2.12}$$

where I_1 and I_2 are two current rms values of the two interferers at ω_1 and $2\omega_1 - \omega_{IM3}$ while $X(\omega_1, \omega_p)$ is a factor which depends only on the relative position between the first interferer and the filter pole[1]. Equation (2.12) displays the same zero at $\frac{\omega_p}{g_m R_S}$ as in the noise transfer function (2.10), showing that noise and linearity are improved according to the same mechanism. The amount of in- band intermodulation given by (2.12) and that obtained using simulations are plotted in Fig.2.6.a, as a function of ω_{IM3} (normalized to ω_p), in the range between 0 and ω_p. As can be seen, a good agreement is obtained over the entire frequency range considered.

In addition to the "pipe" effect, the presence of the capacitor at the input of the stage is key to ensure a high linearity in the presence of far out-of band blockers since it filters out the input interferers before entering the non-linear device. In particular, this effect is related to the capability of the interferers to modulate the gate-source voltage of the input transistor (i.e. the non-linear device). The magnitude of this effect can be estimated calculating the IM3 at a fixed in-band frequency ω_{IM3} as a function of the first blockers position ω_1. Choosing for simplicity $\omega_{IM3} = 0Hz$ (i.e. IM3 product falling at DC) it follows that

$$|I_{IM3}(\omega_1)|^2 \simeq |X(\omega_1, \omega_p)|^2 \, {I_1}^2 I_2 \tag{2.13}$$

The amount of IM3 obtained using (2.13) is plotted in Fig.2.6.b versus ω_1 (also in this case normalized to ω_p). For $\omega_1 \gg \omega_p$, (2.13) can be approximated by the

[1] For $g_m R_S \gg 1, \omega_p < \omega_1$, and the factor X equal to $X(\omega_1, \omega_p) = \frac{3{\omega_p}^3}{4{g_m}^4} \cdot \frac{g_m g_3 (2\omega_1 - j\omega_p) - 2{g_2}^2 \omega_p (\omega_1 - j\omega_p)}{(\omega_1 + j\omega_p)(\omega_1 - j\omega_p)^2 (4{\omega_1}^2 + {\omega_p}^2)}$

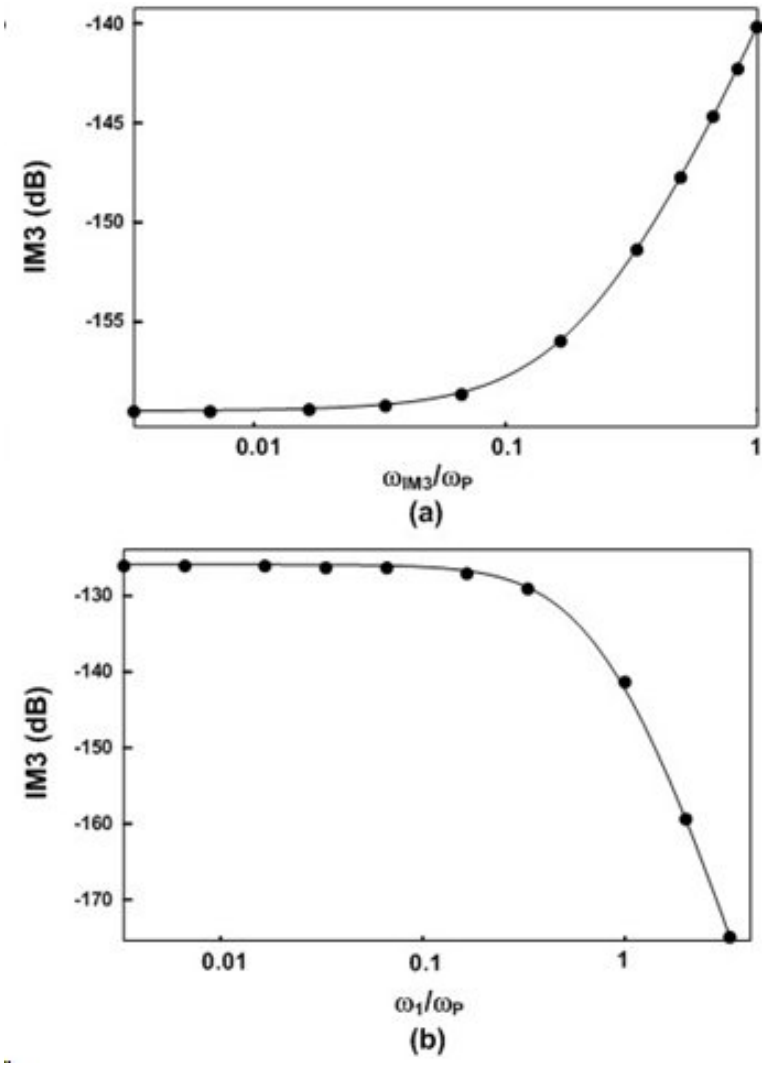

Figure 2.6: 1^{st} Order Filter IM3 (a) versus f_{IM3}, (b) versus f_1 ($\omega_p = 2\pi * 3MHz, g_m = 3.3mS, g_2 = 4.4mA/V2, g_3 = 100\mu A/V3, RS = 20k\Omega$ and $I_1 = I_2 = 135\mu A$). Formulas (line) and simulation (dots)

following expression:

$$|I_{IM3}(\omega_1)|^2 \simeq \left| \frac{3{\omega_p}^3(j g_m g_3 \omega_1 + {g_2}^2 \omega_p)}{8{g_m}^5 R_S {\omega_1}^4} \right|^2 {I_1}^2 I_2 \tag{2.14}$$

where the IM3 product decreases as ${\omega_1}^3$.

The above behavior confirms the intuition, i.e., thanks to the filtering action provided by the input capacitance, the IM3 decreases rapidly when the two interferers are moved further away from the cut-off frequency ω_p. When the interferers fall in the pass-band the gate-source voltage swing is constant and with it the IM3.

This is consistent with the fact that in this region the impedance at the input of the filter does not vary with frequency.

The presence of a passive blocker attenuation in front of the filter is not common to other filter topologies. For example, in standard op-amp RC structures, the current signal injected in the virtual ground is not filtered (as opposed to the voltage output). This forces the operational amplifier to sink or source the same amount of current independently of the position in frequency of the interferer signal with respect to the filter band edge.

2.5 Conclusions

A novel class of filters based on the concept of "pipe filtering" was presented. In the filter pass-band, such kinds of structures behave like lossless pipes where no noise or distortion can be added to the signal. This result in an in-band zero in both noise and IM3 transfer functions and thus in a strong dynamic range increase. Furthermore, passive filtering action provided by the capacitance at the input of the filter improves out-of-band linearity.

Thanks to these properties, such filters can have a greater dynamic range (or equivalently a lower area and power consumption). The "pipe filter" concept will be used in chapter 3 to implement a "pipe" biquad cell that is suitable to build high order filters and to be used in a wireless receiver as a channel selection filter.

Chapter 3

WCDMA Channel Filter with In-Band Noise Shaping

Contents

The real "pipe filter" implementation described in chapter 2 has actually broken the trade-off between the in-band noise and the capacitance value, improving the dynamic range performances, but it has also two noticeable limitations. First of all it has to manage an input current signal and its in-band input impedance could be not adequately low. Second, it can implement only a single real pole and it cannot be used to build high order filters.

In this chapter a "pipe filter" biquad cell is introduced and it is deeply analyzed, with particular focus on noise and lineartity behavior. The pipe filter theory has been also verified by the realization of a 4^{th} order WCDMA channel selection filter prototype. The design process and the measurement results of this integrated filter are described in the last sections of this chapter.

3.1 "Pipe Filter" Biquad Cell

High order filters need both real and conjugate poles. The latter cannot be created by simply cascading two of the structure reported in Fig.2.3. For a given input current signal, a pair of complex poles can be realized through the RLC network shown in Fig. 3.1.a ([15]). In this case the current flowing out from

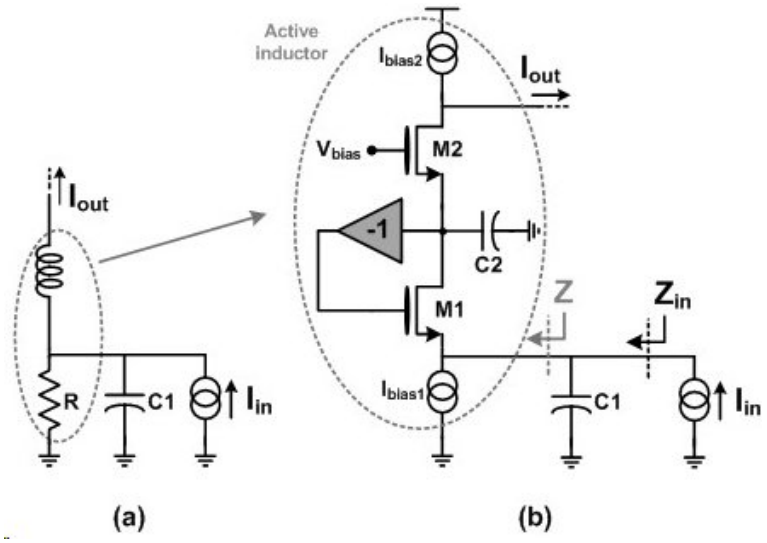

Figure 3.1: Current Biquad Cell

the inductor has a second order low-pass characteristic with a cut-off frequency ω_0 equal to the L-C resonance frequency and a quality factor Q set by the shunt resistance R. Integrated inductors are generally avoided in baseband filters due to the unfeasible value of the inductances required at such frequencies. For this reason, active circuits with an inductive frequency behavior are used (e.g. the gyrator[18]).

3.1.1 Active Inductor

In the proposed biquad cell reported in Fig. 3.1.b, the active inductor is realized through the network formed by transistors M1-M2 and capacitor C2. At DC, the feedback closed around M1 forces the input small signal voltage at the source of M1 to be equal to the difference between the gate-source small signal voltages of M1 and M2, producing (with the use of two identical transistors) a virtual short between the input and the gate of M2. Moving from DC toward higher frequency, the presence of capacitance C2 reduces the amount of feedback around M1 and the input impedance rises as in an inductor. Computing the impedance value of Z

versus frequency under the assumption of $g_{m1} = g_{m2} = g_m$, the following result is obtained:

$$Z = \frac{s\,C2}{{g_m}^2} \cdot \frac{1}{1 + s\,C2\,g_m} \tag{3.1}$$

This behavior corresponds to that of an inductance $L = \frac{C2}{g_{m2}}$ placed in shunt with a resistance $R = \frac{1}{g_m}$. The circuit has literally "gyrated" the impedance $\frac{1}{s\,C2}$ obtaining at its input an inductance of value $\frac{C2}{g_{m2}}$. It can be proved that, in the same way, an inductance connected at the source of M2 would be transformed into a capacitance at the input node.

3.1.2 Conjugate Complex Poles

Thanks to its ability to implement an active inductor, the structure of Fig. 3.1.b realizes a second order low-pass filter with the following transfer function:

$$\frac{i_{out}}{i_{in}} = \frac{{g_m}^2/(C1C2)}{s^2 + s(g_m/C1) + {g_m}^2/(C1C2)} \tag{3.2}$$

where g_m is the transconductance of M1 and M2. The cell has an in-band current gain equal to 1, therefore it is acting as a lossless pipe where no additional current is injected into the signal path. The frequency of the conjugated poles ω_0 and their quality factor Q are given by

$$\begin{cases} \omega_0 = & \frac{g_m}{\sqrt{C1\,C2}} \\ Q = & \sqrt{\frac{C1}{C2}} \end{cases} \tag{3.3}$$

Having chosen the same gm for the two transistors, the biquad cut-off frequency ω_0 depends only on g_m and on the product of the capacitances, while the quality factor Q depends only on the $C1/C2$ ratio.

While the filter transfer function has a low-pass shape, the input impedance of the filter corresponds to that of a LCR shunt resonator and is given by

$$Z_{in} = \frac{s/C1}{s^2 + s(g_m/C1) + {g_m}^2/(C1C2)} \tag{3.4}$$

The band pass shape of the input impedance gives a very low impedance (ideally zero) close to DC (due to the presence of the active inductor) and at extremely high frequencies (due to the capacitance C1). The maximum of the input impedance is located at ω_0 and corresponds to $\frac{1}{g_m}$ (i.e. the shunt loss resistance of the active inductor).

3.2 Biquad Spurious Free Dynamic Range

The spurious free dynamic range of the solution proposed in Fig. 3.1.b was computed valuating the total noise produced by the cell and the amount of distortion generated in the filter pass-band by a couple of interferers located far away from the channel bandwidth. The sources of noise considered were those associated with transistors M1 and M2 and the bias current generator I_{bias1} and I_{bias2} while the distortion was evaluated assuming that the only non-linear elements are transistors M1 and M2.

3.2.1 Noise

Under the assumption of white noise sources and a finite driving resistance $R_S > \frac{1}{g_m}$, the transfer functions from the noise sources associated to transistors M1 and M2 to the output are given by:

$$\left|\frac{i_{out}}{i_{M1}}(\omega)\right|^2 \approx \left|\frac{j\,\omega/\omega_p + 1/(g_m R_S)}{\omega^2/{\omega_0}^2 + j\,\omega/(\omega_0 Q) + 1}\right|^2 \tag{3.5}$$

$$\left|\frac{i_{out}}{i_{M2}}(\omega)\right|^2 = \left|\frac{1-Q^2}{Q}\cdot\frac{j\,\frac{\omega}{\omega_0}\cdot(1+j\,\frac{\omega}{\omega_0}\cdot\frac{Q}{1-Q^2})}{\omega^2/{\omega_0}^2 + j\,\omega/(\omega_0 Q) + 1}\right|^2 \tag{3.6}$$

where ω_0 and Q are given by (3.3) and $\omega_p = \frac{g_m}{C1}$. Both noise transfer functions displays a zero in the filter pass band: the position of these two zero is different for the two transfer functions being a function of R_S for M1 and located in dc for M2.

Fig. 3.2 shows all noise transfer functions for the biquad cell, providing a comparison between theory and simulations. The main difference between the biquad and the first order filter in the transfer function for the noise of M1 is the presence in (3.6) of two complex poles and one zero that produces a pass-band characteristic instead of a high-pass one. This is explained by the fact that the second capacitor C2 filters not only the signal but also the noise injected by M1. On the other hand, a pure high-pass transfer function is present for the noise of M2, since at frequency higher than the poles, capacitor C2 becomes a short and all the noise injected by M2 can flow to the output.

The noise associated with I_{bias1} is injected at the input and thus is processed as the input signal (i.e. without experiencing any attenuation in the filter pass band) while the transfer function of I_{bias2} is flat in frequency since this noise is injected at the output of the cell. In general, these latter contributions are proportional to the transconductance of the transistors used to synthesize the current generators. The shape of the whole output noise spectrum is qualitatively shown in Fig. 3.3.

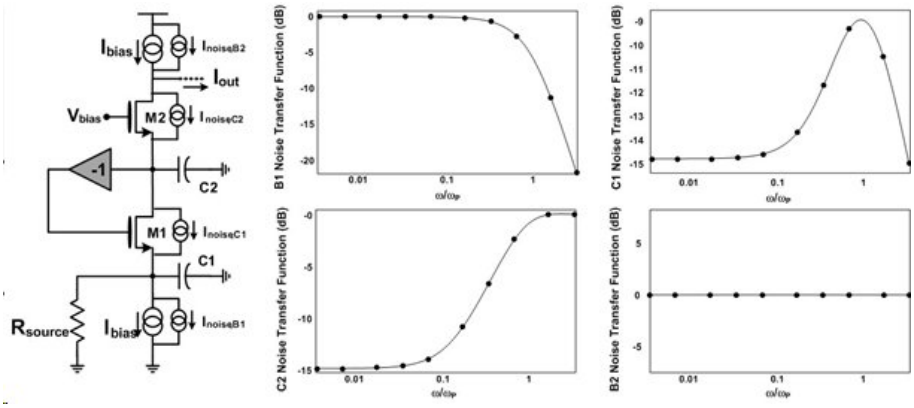

Figure 3.2: Biquad Cell Noise Transfer Functions

At low frequencies the main contributors are the bias generators where noise is not directly related to the filter poles. On the contrary, moving toward the filter

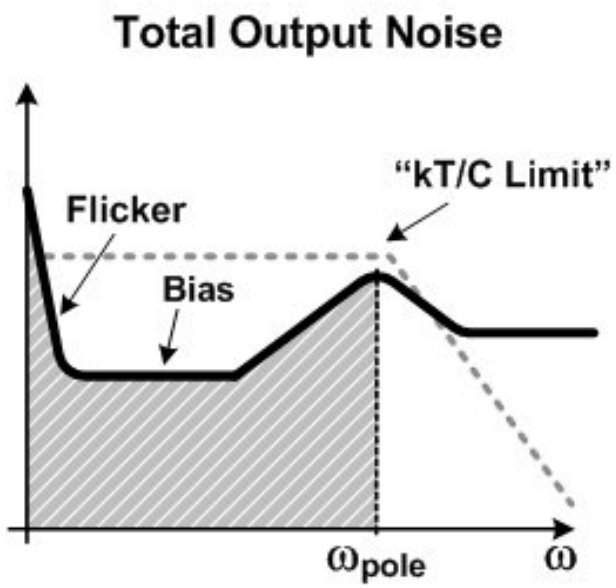

Figure 3.3: Output Noise Summary

cut-off frequency, the noise contributed by M1 and M2 increases reaching its maximum at ω_0 where their noise spectral density is close to the one of classical filter topologies. Beyond the filter cut-off frequency, the only noise components that are not filtered out are those due to M2 and to the upper bias current generator. This out-of-band noise, as it will be explained in section 3.3.2, must be carefully considered because it can be folded in band when the signal is sampled at the end of the analog receiver chain, typically by an ADC.

3.2.2 Intermodulation Phenomena

As seen in Section 2.4.2, the "pipe filters" allow to obtain high linearity taking advantage of two different mechanisms. The first is the same mechanism that produces the in-band high-pass noise shaping while the second is the filtering action provided by the input capacitance. As it was done for the first order filter, these two effects were studied also for the biquad cell, evaluating the IM3 generated by two out-of band blockers I_1 and I_2 for two different scenarios. In the first, the frequency of the intermodulation product ω_{IM3} is made to vary within the pass band by placing I_1 at ω_1 and I_2 at $2\omega_1 - \omega_{IM3}$. In the second, intermodulation product ω_{IM3} is made to always fall at DC placing I_1 at ω_1 and I_2 at $2\omega_1$, while ω_1 is made to vary. Contrary to the first order filter, where the transistor output resistance is in shunt with the transconductance and thus its impact on linearity is negligible, in this case the finite output resistance (not considered in the Volterra's analysis) affects the linearity of the cell by modifying the behavior of the feedback loop used to realize the active inductor. For this reason in Fig. 3.4, simulations with output resistance were also reported. Analyzing the case in which the IM3 product is made to vary across the band (Fig. 3.4.a), it can be seen that in the frequency range for which the virtual ground provides a very low impedance almost all the input current flows towards the output and low distortion is produced. This behavior is equivalent to the one of the first order filter reported in Fig. 2.6.a.

In Fig. 3.4.b, the IM3 is plotted as a function of the first blocker position ω_1 showing a pass band behavior. As in the first order topology (section 2.4.2), the IM3 frequency behavior follows the input impedance profile given by (3.4): rising up with frequency in the filter pass band (inductive behavior), and decreasing with frequency out of band (capacitive behavior). The worst distortion occurs at the corner frequency, where the input impedance and the modulation across the input transistor reach their maxima.

3.2.3 Hard Distortions

To fully characterize the linearity of the biquad cell, also hard distortions have to be analyzed. These non-linearities can influence the 1dB compression point of the cell and occur when the signal current becomes comparable with the bias level. Thus, the higher is the bias current, the higher is the capability to handle large signal without a significant compression. Also in this case the filtering action of input capacitance C1, plays an important role and gives this filter an advantage with respect to other classical architectures. In fact, the current due to the largest input signals, typically located outside the channel bandwidth, is primarily

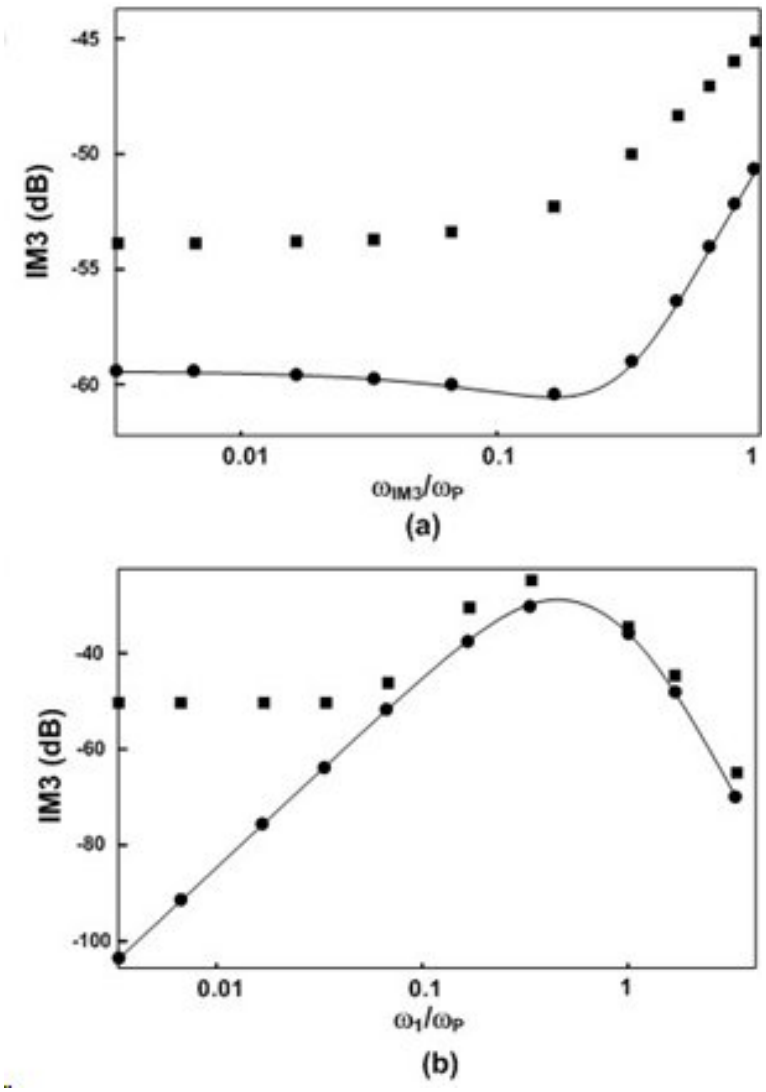

Figure 3.4: Biquad Cell Stage IM3 (a) versus f_{IM3}, (b) versus f_1 ($\omega_p = 2\pi * 3MHz, Q = 0.54, g_m = 3.3mS, g_{m,2} = 14.4mA/V^2, g_{m,3} = -79\mu A/V^3, R_S = 1.66k\Omega$ and $I_1 = I_2 = 135\mu A$). Formulas (line) and simulation with and without finite transistor output resistance (square and dots respectively)

absorbed by C1. This reduces the current entering in the filter with a consequent enhancement of the 1dB compression point.

In conclusion, the current mode biquad cell proposed has two important properties making it very suitable for use in a receiver chain. First, it achieves low noise in the signal band, where a high signal-to-noise ratio is the key target. Second, its

linearity increases as the input signal is moved far away from the band edge. This latter behavior fits the linearity requirement of a typical wireless receiver where most of the input signal power is located out-of-band (interferers)[19]. Furthermore the interferer power tends to increase proportionally to its distance from the filter band edge (channel bandwidth).

3.3 Design of 4^{th} WCDMA Channel Selection Filter

To validate the theory reported above, a 4^{th} order Butterworth filter intended to perform channel selection in a WCDMA receiver was designed and integrated in $65nm$ CMOS technology ([15],[13]). The filter was implemented as the cascade of two current biquad cells like the one of Fig. 3.1 (adopting a fully-differential architecture to easily implement the sign inversion in the feedback network). A complete scheme of the structure is drawn in Fig. 3.5. The filter was designed to

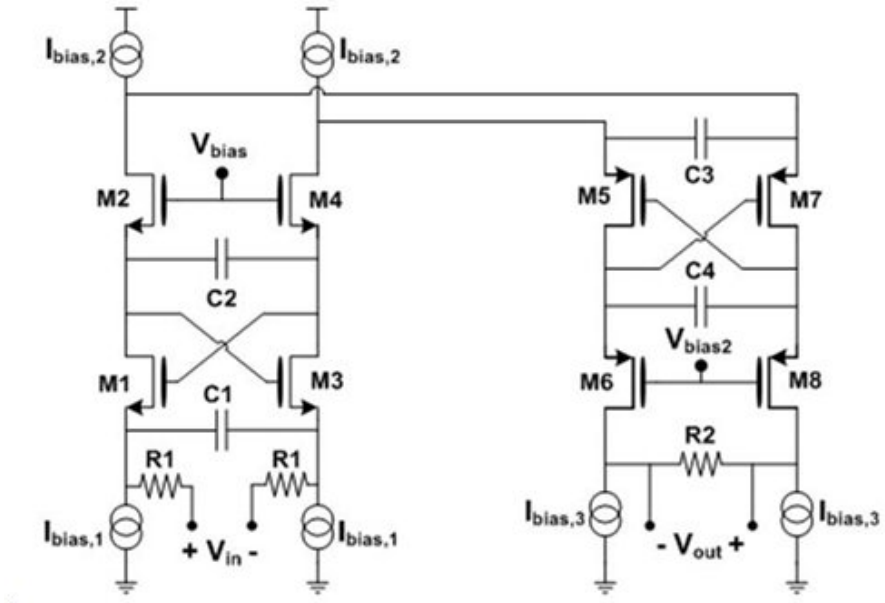

Figure 3.5: 4^{th} Order Filter Schematic

operate after a current mixer that, for its nature, behaves as a current signal source. In this case, however, for testing purpose, two resistances (R1) were connected to the input to implement a V-I converter. This was possible since this structure has a very low in-band input impedance. Also for ease of testing, the output current was converted to voltage on the differential resistor R2. The relative noise contribution of R2 decreases as R2 is increased. In fact, while the noise added by

R2 is proportional to its value, all the other contributes are amplified by the square of R2. The maximum feasible value for R2 is limited by the maximum swing at the cell output. However, most of the input energy is located out of band and it is filtered out before reaching R2. As a consequence R2 can be chosen sufficiently high ($20k\Omega$) to make its noise contribution negligible (less than 2% of the total).

3.3.1 Design Strategies for "Pipe Filter" Cascade

One of the first steps in a filter design is the choice of the cut-off frequency ($\omega_{cut-off}$). In classic filters, where noise and signal have roughly the same transfer function, this frequency is generally minimized to maximize the blockers attenuation. Indeed, a higher $\omega_{cut-off}$ would not produce any benefit on the in-band SNR, since both the noise and the signal are processed by the same transfer function [3]. For a "pipe filter" however, the presence of in-band noise shaping makes this choice less obvious, as it is qualitatively shown in Fig. 3.6. If $\omega_{cut-off}$ is

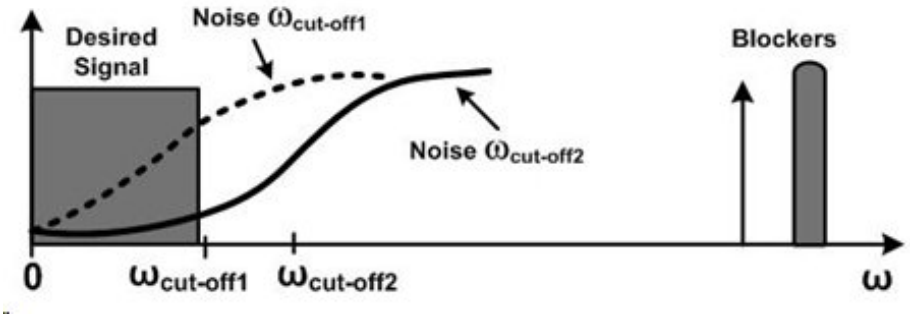

Figure 3.6: Choice of Cut-Off Frequency

moved beyond the channel bandwidth, due to the difference in the noise and signal transfer functions a significant improvement of SNR is produced. However this benefit trades off with the requirements of selectivity that depends on the position and on the amplitude of the input interferers. In the case of a WCDMA receiver, the scenario considered by the standard assumes the presence of two interferers at $10MHz$ and $20MHz$, with well defined energies [19]. On the base of these requirements a compromise $\omega_{cut-off} = 2.8MHz$, that is 1.45 times the channel bandwidth (i.e. $1.92MHz$), was chosen.

The second step in the filter design is the definition of the bias current for each stage. This value must be greater or equal to the largest between the minimum current necessary to handle the interferers and the minimum current that allows to satisfy the condition $g_m \gg \frac{1}{R_S}$ required for a proper operation of the filter

(see Section 2.4). Although in general the first condition is the more stringent, the use of a mixer as driving stage could require a higher bias current to keep negligible the effect of the finite impedance of the down-converter on the filter transfer function [20]. In this design, since the input capacitance C1 attenuates the blocker at $10MHz$ by almost $10dB$ and the one at $20MHz$ by almost $16dB$ (being $\omega_{cut-off} = 2.8MHz$), the bias current can be three time smaller than the one that would be required to manage the full interferer. For the same reason, the bias current of the second stage can be reduced by another factor of ten since the $10MHz$ blocker is attenuated by an additional $20dB$ by the first stage. The minimum bias current required by the second stage is lower also because the first stage provides an output impedance larger than R_S (i.e. $R_S \cdot (\frac{g_m}{g_{ds}})$).

The final step is to choose the transconductances and the capacitances of the cell that minimize the noise and maximize the signal voltage swing compatibly with the supply voltage. The impedance levels can be increased moving down the filtering chain because each stage increases the driving impendence for the following stage and contributes in the filtering of out of band interferers. The impedance scaling gives also a reduction of the silicon area since smaller capacitances are needed. For the solution proposed, the transconductances of the two stages have been set respectively to $3.3mS$ for the first cell and $330\mu S$ for the second one.

In Tab. 3.1 the design parameters for all transistors are reported. Notice that, the overdrive of the current generators is much larger than that of M1-M2 to minimize their contribution to the in-band noise.

	I_{bias} Current $[\mu A]$	W/L $[\mu m/\mu m]$	Overdrive Voltage $[mV]$	g_m $[mS]$
$I_{bias,1}$	240	24/10	764	0.565
M1/M2/M3/M4	240	144/2	110	3.35
$I_{bias,2}$	264	132/10	715	0.664
M5/M6/M7/M8	24	12/0.5	131	0.34
$I_{bias,3}$	24	24/10	219	0.2

Table 3.1: Filter prototype transistors parameters

3.3.2 Out-band Noise Folding

The out-of-band noise present at the output of a "pipe filter" can be folded down during the sampling phase that occurs within the ADC. For this reason this noise has to be minimized to maintain an advantage compared to traditional solutions,

where most of the noise lies in the filter pass band.

The out-of-band noise in a "pipe filter" is contributed only by the last stages of the filtering chain that have a high-pass transfer function (e.g. the noise of M2 and of I_{bias2} in Fig. 3.2). This noise is proportional to the bias current that, as shown in the previous section, is scaled down in the last stage. Finally, since in general the current signal has to be converted to voltage before entering the ADC, an additional pole can be added at the end of the "pipe filter", placing a capacitor in parallel with the load resistance, providing a further attenuation of the out-of-band noise. Introducing this additional pole does not require a large capacitance since a large resistor can be used at the output where most of the interferers are already filtered.

Due to the above, in the proposed design the out-of-band noise (obtained integrating it from the filter corner $\omega_{cut-off}$ to "infinite") is less than one third of the in-band noise. This means that, even sampling the output at the Nyquist rate, which is rarely done, the in-band noise after sampling would increase less than $1dB$.

3.4 Device Test

The chip micrograph of the filter prototype ([15]), fabricated in a $90nm$ CMOS process, is shown in Fig. 3.7. All pads are ESD protected and the active die area is $0.5mm^2$. This area is dominated by low-density MiM capacitors ($210pF$), whose placement could be further improved, resulting in a lower area occupation. Moreover large on-chip MoM bypass capacitors are used to filter the noise on the supply voltage with respect to ground. The die was bonded on a dedicated double side RF board, realized on an $FR4$ substrate. Gold strip lines, optimized to reduce their area occupation, carry the signals from the input connectors to the die. As discussed in the previous section, the voltage to current conversion is performed placing two resistances (R1) of $1.66k\Omega$ in series with the input while the output signal is sensed on a resistor (R2) of $20k\Omega$. The plot of the filter frequency response versus frequency from DC to $20MHz$ is shown in Fig. 3.8 together with the response of the ideal 4^{th} order Butterworth filter used for the design. The plot is obtained de-embedding the effect of the parasitic pole caused by the capacitive load associated with the probe (about $5pF$). The DC gain is about $15dB$, due to the ratio between the output and the input resistors, and the filter cut-off frequency is close to $2.8MHz$ as expected from the simulations. When the out of band attenuation reaches about $55dB$ the plot levels off due to a parasitic leakage on the board. This was proved by measuring the input to output

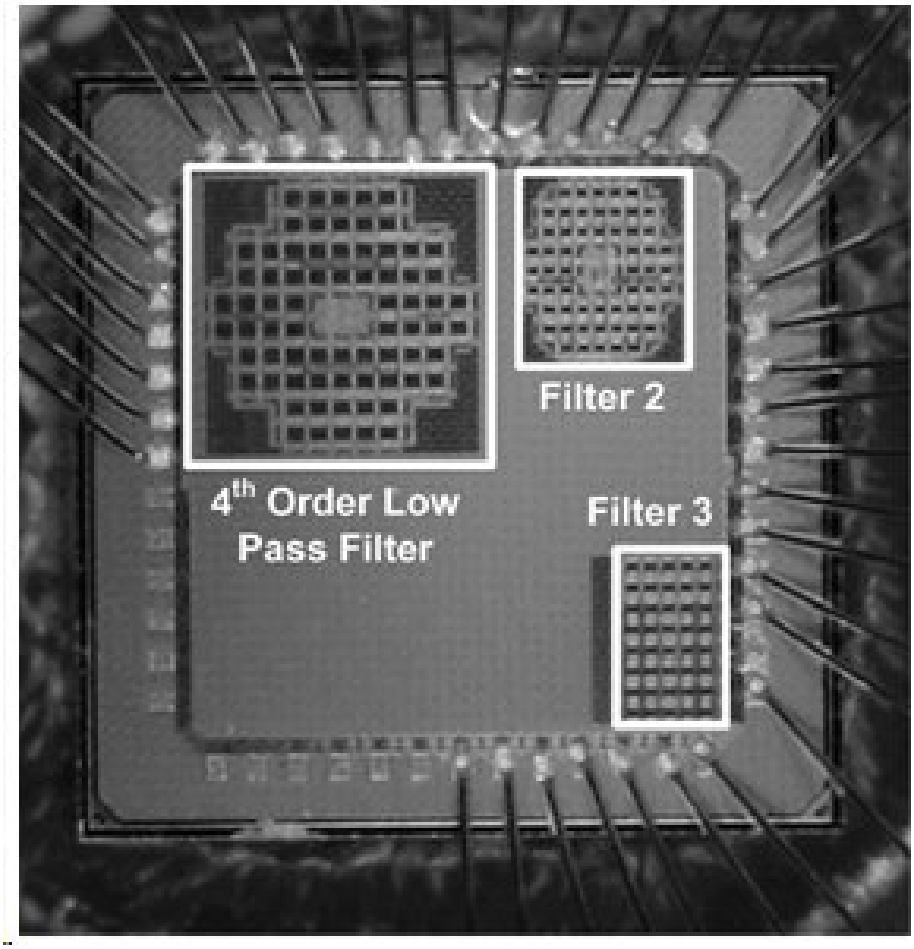

Figure 3.7: Chip Micrograph

transfer function with the filter powered off.

The output noise spectrum was measured shorting the differential inputs of the die in front of the R1 resistance. In this way the effect of the finite driving impedance (i.e. the output resistance of the mixer in a receiver chain) on the filter output noise is included. At the receiver output an active probe with a $20dB$ gain was used to raise the filter noise above the sensitivity level of the spectrum analyzer. The measured output noise spectrum is reported in Fig. 3.9 compared with the simulated one. The noise transfer function has a band pass shape as expected from the theory. The noise spectrum shows a minimum equal to $-128.5dBm/Hz$, located in the filter band, where the main contributors are the bias generators. Below that $1/f$ noise dominates while near the corner frequency, where the main contributors are the filtering transistors, there is a local maximum equal to $-123dBm/Hz$. At higher frequencies the output noise decreases be-

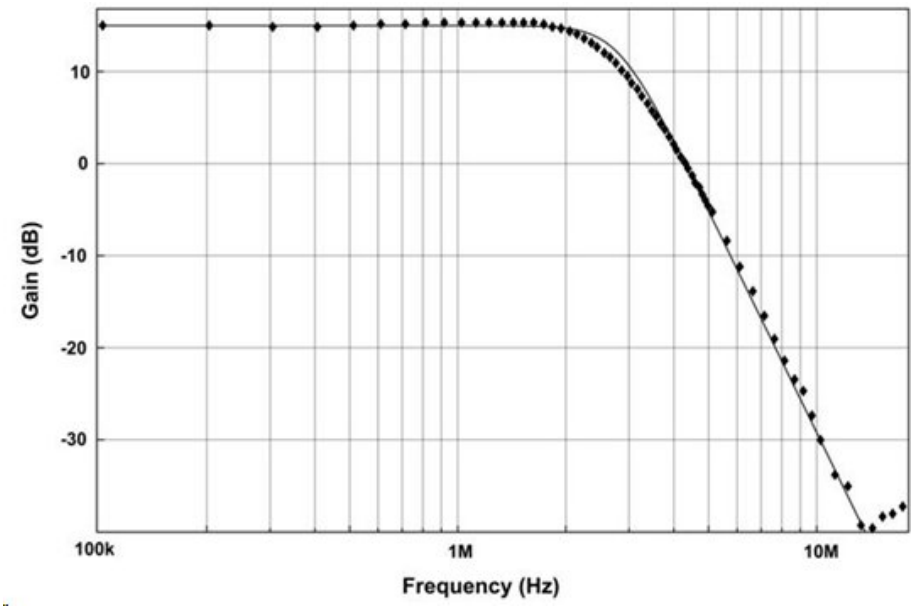

Figure 3.8: Measured Output Transfer Function

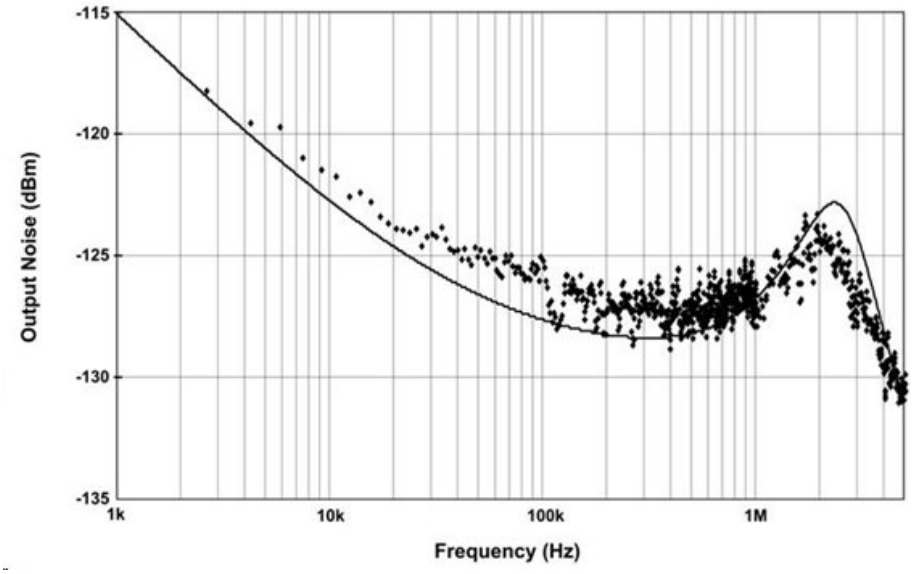

Figure 3.9: Measured Noise Transfer Function

cause all contributors are filtered out by the filter itself and by the parasitic output pole. The $1/f$ corner is located at $25kHz$. This output noise frequency behavior is consistent with the theory, as shown by the solid line in Fig. 3.9. The out-of-band IIP3 is $35.6dBm$, and it has been measured with two tones, the first placed at $10MHz$ and the second at $19.5MHz$, that give a 3^{rd} order intermodulation

product at $500kHz$. Fig. 3.10 shows the simulated (dots) and measured (squares) filter IIP3, vs. the frequency of the IM3 product (Fig. 3.10.a) and vs. the frequency of the first blocker f_1 (Fig. 3.10.b). These frequencies are kept the same, with respect to the plots in section 3.2.2. The measurements fit very well with the simulations, confirming the theory.

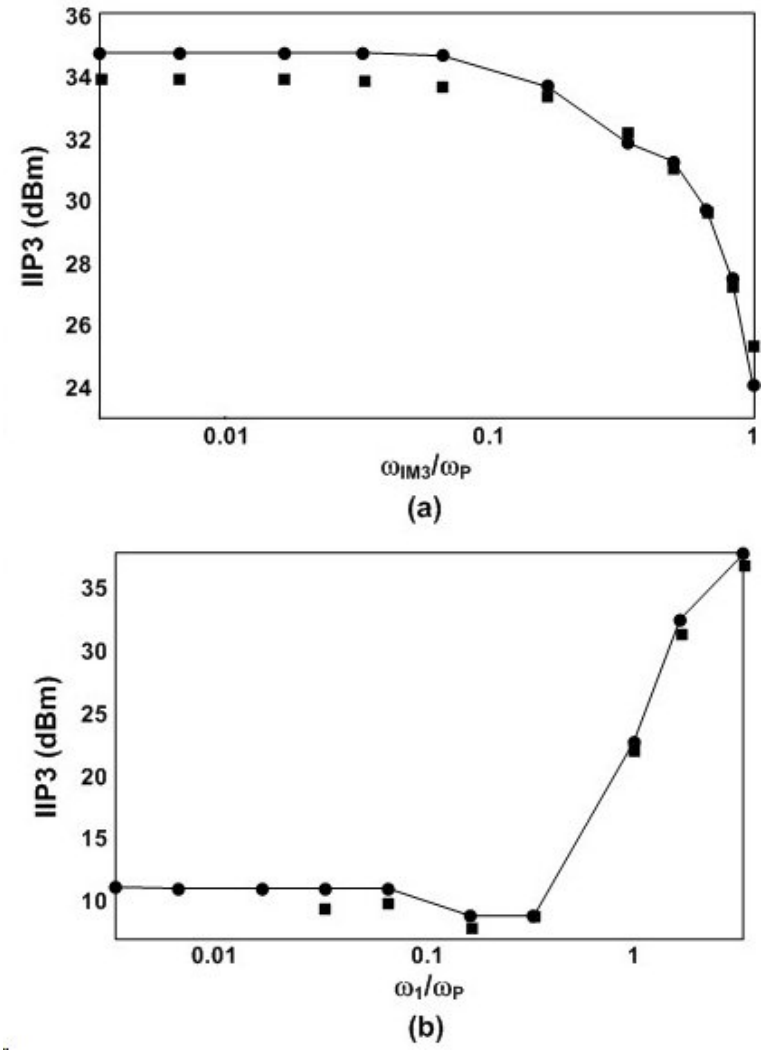

Figure 3.10: 4^{th} Order Filter IIP3 (a) versus f_{IM3}, (b) versus f_1. Simulation (dots) and measurements (squares)

A summary of the most relevant measurements and a comparison with the state of art for filters designed for the same applications (WCDMA) is reported in Tab. 3.2. In particular this work has the lowest power consumption, equal to $1.26mW$, with a spurious free dynamic range (SFDR) higher than all but one of

	This Work	[3]	[1]	[5]	[6]	[7]
Voltage Supply $[V]$	2.5	1.2	2.7	1.8	2.5	1.2
DC Power $[mW]$	1.26	3.4	6.21	4.86	7.3	1.8
Cut-freq$[MHz]$	2.8	2.11	1.92	2	2.2	2.75
Number of Poles	4	4	5	5	3	5
IIP3 Out of Band $[dBm]$	35.6	31	41	33	15	24
Input referred noise $[\mu V_{RMS}]$	32	36	47	80	52	116
SFDR Out of band $[dB]$	75	71.25	76.5	68	58.5	59.75
FoM $[dB]$	-174	-165	-168	-161	-148	-159

Table 3.2: Filter prototype Measurements and Comparison with the State-of-the-art

the other filters. The filter cut-off frequency is set to $2.8MHz$, i.e. about40% larger than the UMTS bandwidth that is equal to $1.92MHz$. This gives a significant in-band noise improvement while still providing sufficient selectivity. Finally the Figure of Merit (FoM)[1] (based on [1]) is almost $6dB$ better than the next best one.

Two more versions of the filter were also fabricated, where the capacitors are scaled down by a factor of six (Tab. 3.3). One of these scaled filters (called filter

	Filter 2	Filter 3
Voltage Supply $[V]$	2.5	1.8
DC Power $[mW]$	0.21	0.15
Cut-freq$[MHz]$	2.8	2.8
Number of Poles	4	4
Gain $[dB]$	-1	-7
IIP3 Out of Band $[dBm]$	40.7	48.5
Input referred noise $[\mu V_{RMS}]$	126	273
SFDR Out of band $[dB]$	70.43	71.18
FoM $[dB]$	-178	-180

Table 3.3: $2.5V$ (filter 2) and $1.8V$ (filter 3) scaled versions

2) is operated from a $2.5V$ supply while the other (called filter 3) is operated from a 1.8 supply. Filter 2 uses input resistors scaled up by a factor slightly higher than 6 and has a slightly better FoM than the un-scaled filter. For the case of filter 3, the input resistors are increased close to the maximum feasible value which still allows to reach full scale swing at the output without exceeding the supply with the input signal. In this situation a much greater linearity is obtained together with

[1] $FoM = \frac{\text{Power Dissipation}}{(\text{no. of poles}) \times (\text{cut-off frequency}) \times \text{SFDR}}$

a relatively small increase in noise. This results in a further improvement of the FoM ($2dB$ with respect to filter 2, $6dB$ with respect to the un-scaled filter and $12dB$ with the respect to the state of art).

3.5 Conclusions

The "pipe filter" concept has been used to build a biquad "pipe filter" cell having low in-band input impedance and showing all the "pipe filter" properties introduced in chapter 2, in terms of noise and linearity. This biquad cell has been used to build a 4^{th} order low pass filter prototype, designed to fit the WCDMA channel selection filter specifications. This filter prototype has been tested in order to validate the "pipe filter" theory and it has been compared to the WCDMA channel selection filters state-of-the-art. The present filter shows significant results in terms of low power consumption and high spurious free dynamic range. In particular a Figure of Merit has been used to evaluate this comparison quantitatively, showing a $6dB$ improvement with respect to the state-of-the-art.

Chapter 4

A Current-Based Reconfigurable Front- End for GSM and UMTS Standards

Contents

The "pipe filter" concept introduced in chapter 2 is definitely suitable to implement a channel selection filter topology for an entirely current-based receiver front-end. This is because a "pipe filter" manages current signals both at the input and at the output. Furthermore its combination of low in-band noise and high out-of-band linearity is very appropriate for a wireless receiver base-band filter, because it maximizes the dynamic range just where the specs are more constraining.

In order to design a current-based reconfigurable front- end for GSM and UMTS, the receiver specs for both configuration have been derived from the standard definition documents. In the remaining sections of this chapter the receiver blocks are described, with particular focus on the baseband channel selection filter. Finally, all the simulation results are reported, in order to show the front-end performances for both standard GSM and UMTS configurations.

4.1 GSM and UMTS Standard Specifications

4.1.1 GSM General Features

The Global System for Mobile communications (GSM) is the most popular standard for 2G mobile telephony systems. The GSM standard sets several performances that must be satisfied by the receiver front-end ([21]). In every test are set the signal input power and their frequency position. In particular a test is said to be satisfied if the receiver can detect the signal with a Bit Error Rate (BER) lower than or equal to 10^{-4}. Furthermore, starting from the requirements knowledge, it is possible to derive all the parameters that are necessary to design the receiver, such as NF, IIP2 and IIP3. This values will be referred at the receiver input (i.e. the antenna), before the Sourface Acoustic Wave (SAW) filter, that is usually the first block in a receiver chain.

Main Standard Specifications

The GSM standard defines several frequency bands, one for each GSM version (or GSM family). The two bands included in the european standard are GSM $900MHz$ and DCS $1800MHz$, with the following frequency ranges:

- Standard GSM $900MHz$
  - $890 - 915MHz$ communication from Mobile Station (MS) to Base Transceiver Station (BTS)
  - $935 - 960MHz$ communication from BTS to MS
- DCS $1800MHz$
  - $1710 - 1785MHz$ communication from MS to BTS
  - $1805 - 1880MHz$ communication from BTS to MS

More than the two main frequency bands, also the following bands have been defined:

- GSM $450MHz$
  - $450.4 - 457.6MHz$ communication from MS to BTS
  - $460.4 - 467.6MHz$ communication from BTS to MS
- GSM $480MHz$
  - $478.8 - 486MHz$ communication from MS to BTS
  - $488.8 - 496MHz$ communication from BTS to MS
- GSM $750MHz$
  - $747 - 762MHz$ communication from MS to BTS
  - $777 - 792MHz$ communication from BTS to MS
- GSM $850MHz$
  - $824 - 849MHz$ communication from MS to BTS
  - $869 - 894MHz$ communication from BTS to MS
- Railway GSM $900MHz$ (R-GSM)
  - $876 - 915MHz$ communication from MS to BTS
  - $921 - 960MHz$ communication from BTS to MS
- Extended GSM $900MHz$ (E-GSM)
  - $880 - 915MHz$ communication from MS to BTS
  - $925 - 960MHz$ communication from BTS to MS
- Personal Communication System (PCS) $1900MHz$
  - $1850 - 1910MHz$ communication from MS to BTS
  - $1930 - 1990MHz$ communication from BTS to MS

All over the world, different countries use different GSM bands.

The GSM is a multiple access system, both time division (TDMA) and frequency division (FDMA). In particular, the GSM is a Time Division Duplex - Frequency Division Duplex (TDD-FDD) system: the communication from MS to BTS is divided form the communication from BTS to MS both in time and frequency. In fact the two communications use different time ranges and different frequencies.

Sensitivity Test

The sensitivity is defined as the minimum signal level that the system can detect with acceptable signal-to-noise ratio (SNR) ([22]). The GSM standard provides a $-108dBm$ sensitivity with a $4dB$ overall SNR for the TCH/FS configuraton and a $-102dBm$ sensitivity with a $7dB$ overall SNR for the TCH/HS.

These SNR values are computed to have a $BER < 10^{-4}$ in static channel condition, with an optimum demodulator MLSE (Maximum Likelihood Sequence Estimation) for the GMSK modulation. On the contrary, with a sub-optimum MSK modulator, the required SNR can be 1-2dB higher. This configuration can be interesting for low power receiver configurations.

Noise Figure

The noise factor is defined by

$$F = \frac{SNR_{in}}{SNR_{out}} \tag{4.1}$$

where SNR_{in} and SNR_{out} are the input and output signal-to-noise ratios of the considered network. The noise figure is just the dB value of the noise factor, and it can be calculated as

$$NF = 10Log_{10}F \tag{4.2}$$

Starting from the definition of (4.2) and assuming an optimum demodulator for the TCH/HS configuration it can be derived

$$NF = SNR_{in}|_{dB} - SNR_{out}|_{dB} = S_{in}|_{dBm} - N_s|_{dBm} - 7dB \tag{4.3}$$

where

- $S_{in}|_{dBm}$ is the receiver required sensitivity, thus $-102dBm$
- $N_s|_{dBm}$ is the thermal noise of the source resistance R_S at the network input. Assuming an input matching, it is computed as

$$N_s = \frac{(V_{noise}/2)^2}{R} = \frac{4kTR_sB}{4R_s} = kTB \tag{4.4}$$

  Since the GSM channel bandwidth is $B = 200kHz$, $N_s = -120.8dBm$.

The input referred noise figure required for a GSM receiver is therefore $11.8dB$.

Intermodulation Test

The intermodulation test requires that the receiver is able to detect the input signal with the desired SNR (i.e. 7dB) when at the receiver input are present at the same time:

- The desired signal at f_0 frequency with an input power 3dB greater than sensitivity (i.e. -99dBm)
- A continuous sine wave at frequency $|f_1 - f_0| = 800kHz$ with a $-49dBm$ power
- A GMSK modulated signal at frequency $|f_2 - f_0| = 1.6MHz$, also with a $-49dBm$ power

The third order intermodulation product (IM3) generated by the two interfering signals falls exactly at f_0 frequency, decreasing the SNR.

The receiver $IIP3$ specification can be derived from the intermodulation test. In fact, the $IIP3$ can be computed with the following formula ([22]):

$$IIP3|_{dBm} = \frac{1}{2}(3P|_{dBm} - IM3|_{dBm}) \tag{4.5}$$

where P is the intermodulation power ($-49dBm$ in this case) and $IM3$ is the third order intermodulation product that is generated at f_0 frequency. Thanks to the (4.5) it can be derived the receiver $IIP3$ specification of $-18.5dBm$.

AM suppression Test

Although the GMSK modulation is a costant envelope modulation, the GSM standard requires a test called "AM suppression test". To satisfy this test, the receiver must be able to detect the input signal with the desired SNR when at the receiver input are present at the same time:

- The desired input signal with a GMSK modulation, at f_0 frequency, with an input power 3dB greater than sensitivity (i.e. -99dBm)
- A GMSK modulated signal at frequency $|f - f_0| = 6MHz$ with a -46dBm power.

The interfering signal can generate, in presence of second order distortion, a second order intermodulation product centered at DC frequency and with a bandwidth two times larger than the interferer's one. This AM suppression test has

been introduced to avoid the signal desensitization in presence of a pulsed GMSK interfering signal, produced by an on-off transition of the TDMA signal.

The receiver IIP2 specification can be derived from the AM suppression. In fact, the IIP2 can be computed with the following formula ([22]):

$$IIP2|_{dBm} = 2P|_{dBm} - IM2|_{dBm} \tag{4.6}$$

where P is the intermodulation power ($-46dBm$ in this case) and $IM2$ is the second order intermodulation product that is generated. Thanks to the (4.6) it can be derived the receiver $IIP2$ specification of $14dBm$.

Blocking Tests

This test requires that the receiver is able to detect the input signal in presence of a blocking continuous sine wave, with the desired SNR. The test scenario requires an input signal at f_0 frequency with a power $3dB$ greater than the sensitivity, and provides the following blocker cases:

- A $-43dBm$ wave at $|f - f_0| = 600kHz$
- A $-33dBm$ wave at $|f - f_0| = 1.6MHz$
- A $-26dBm$ wave at $|f - f_0| = 3MHz$
- A $-20dBm$ wave at $|f - f_0| = 20MHz$ (out of band interferer)

The influence of these tests is very important to set the tolerable signal swing for all the single blocks of a receiver, because they can saturate the circuits and thus they can reduce the receiver performances.

Adjacent and Alternate Channels

In the GSM standard, the adjacent channel is $200kHz$ far from the input signal, while the alternate channel is $400kHz$ far. The standard requires a test where the input signal (C) is a GMSK modulated wave with a power $20dB$ greater than the sensitivity and the adjacent channel (I_1) and the alternate channel (I_2) are present at the same time. Also these waves are GMSK modulated signals with a $200kHz$ bandwidth. Moreover, the test defines the carrier-to-interferer ratios as

$$\frac{C}{I_1} = -9dB \tag{4.7}$$

$$\frac{C}{I_2} = -41dB \tag{4.8}$$

The calculated signal powers are reported in Tab. 4.1

Signal	Power [dBm]
Desired Signal	-82
Adjacent Channel	-73
Alternate Channel	-41

Table 4.1: Adjacent and Alternate Channels Test

As the blocking test, also the adjacent and alternate channel tests are important to set the tolerable signal swing for all the single blocks of a receiver.

Maximum Signal Test

This test defines the maximum input signal that a GSM receiver must be able to detect, by keeping the desired SNR. This signal is $-25dBm$.

4.1.2 UMTS General Features

The Wideband Code Division Multiple Acces (WCDMA) ([19], [23]), also known as UMTS/FDD or UTRA/FDD, is the interface standard for 3G mobile telecommunication networks. 3G WCDMA systems have a lot of differences with respect to the 2G TDMA/FDMA ones.

First, rather than being separated in frequency or time, users are now separated by orthogonal codes. As the use of codes implies a spectral spreading, the treatment of overall signal-to-noise ratio requires considerations that are different from those required for TDMA systems. Second, a single radio channel behaves more like band-limited noise than a single sinusoid. Statistical terms like peak-to-average power ratio are therefore necessary to reflect this new constellation of signals.

General characteristics of the UTRA/FDD system are listed in Tab. 4.2. The

Parameter	Specification
Uplink Frequency Band (TX) [MHz]	1920to 1980
Downlink Frequency Band (TX) [MHz]	2110to 2170
TX to RX Frequency Separation [MHz]	45 to 190
Nominal Channel Spacing [MHz]	5
Chip Rate [Mcps]	3.84

Table 4.2: UTRA/FDD WCDMA System Characteristcs

nominal frequency spacing between adjacent channels is $5MHz$ and the signal

bandwidth is $3.84MHz$ (corresponding to the chip rate). The downlink employs quadrature phase-shift keying (QPSK) modulation. Root-raised-cosine filtering is applied to shape the spectrum. Using orthogonal spreading and gold-code scrambling, several CDMA channels are multiplexed onto the same frequency channel. Hence, the received signal consists of many simultaneously transmitted channels that use the same carrier frequency. As a result, large amplitude variations occur over time. The uplink is similar but uses a more complicated hybrid-QPSK modulation scheme. Although a combination of code allocation and complex scrambling is used to minimize the number of signal nulls, the envelope of the transmitted signal continues to display large amplitude variations. These variations place high linearity requirements on the power amplifier, which is believed to be a major RF design challenge.

Processing Gain

The UMTS standard describes a number of test scenarios in which the user bit rate is fixed at $12.2kbps$ and the bit error rate (BER) must be below 10^{-3}. The desired downlink channel signal includes two or more orthogonal CDMA channels, which comprise the dedicated physical channel (DPCH) carrying the user data, a synchronization channel and, in some cases, other users' data channels. The standard specifies total power levels within the channel bandwidth and the relative level of the DPCH. For simplicity, the desired channel power is specified as the DPCH channel power throughout this article.

In the baseband receiver, the despreading process concentrates the desired signal energy in a bandwidth that corresponds to the channel symbol rate. Since noise and interference are uncorrelated with the despreading code, noise is not concentrated in a smaller bandwidth. Further, signal decoding results in a coding gain, and the total resulting improvement in signal-to-noise ratio is defined as the user data processing gain given by

$$G_P = 10log_{10}(\frac{3.84Mcps}{12.2kbps}) = 25dB \tag{4.9}$$

However the chosen definition facilitates a more general comparison of different systems. The required minimum E_b/N_t[1] for a BER of 10^{-3} is determined from simulations to be $15.2dB$. The term E_b/N_t is used here instead of the traditional notation E_b/N_0 since most tests include interference in addition to noise. It is also suggested that an implementation margin has to be added to account for various

[1] E_b/N_t is the ratio of average bit energy to noise and interference power spectral density

baseband imperfections. The required effective E_b/N_t (including an implementation margin) is then expressed as

$$\left(\frac{E_b}{N_t}\right)_{eff} \approx 17dB \tag{4.10}$$

wich complies with the chosen definition of processing gain.

Transmitter Leakage and Sensitivity

Until the new 3G system delivers the coverage and services offered by the well-established 2G systems, multimode terminals with both 2G and 3G capabilities are required. Such a transceiver system configured for two wireless systems is shown in Figure 1. In the transceiver system, a system select switch is used for selection

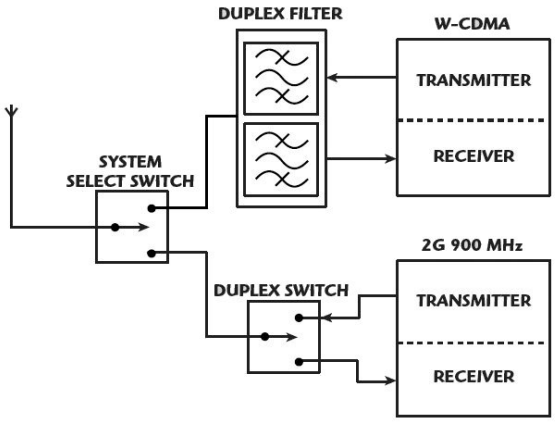

Figure 4.1: Example of a Duplex Arrangement of a Mobile Transceiver Unit including 3G WCDMA and 2G TDMA System([19])

between a 2G $900MHz$ system (EGSM) and a 3G WCDMA system. The 2G system applies time division duplex (TDD) as well as frequency division duplex (FDD), and a duplex switch is used to select transmit or receive modes. Since the considered WCDMA system only applies FDD and thus employs simultaneous transmission and reception, a duplex filter is required to provide isolation between the transmitter and the receiver. The continuous presence of the high power transmitter signal causes problems with spurious leakage from the transmit band located at a 45 to $190MHz$ offset. Unless sufficient selectivity is available between the Tx and Rx bands, this spurious transmitter signal will cause severe dynamic range and intermodulation problems in the receiver chain.

Therefore, it should be clear that a high performance duplex circuit with good TX-RX isolation is needed. Based on data for switches and ceramic duplex fil-

ters available commercially today, an estimate of duplex circuit performance can be guessed. The loss in the receive path can be up to $4dB$ and it has severe implications for the overall noise figure, however, since a small physical size is mandatory, it appears inevitable. The power level of the transmitter leakage signal at the receiver input is determined by taking the transmitter power class, adding the specified tolerance, adding the transmit path loss ($2.5dB$) and subtracting the expected duplex filter isolation. The result is between -21 and $-25dBm$: the receiver must be able to handle this signal without significant performance degradation.

The minimum signal power that must be detectable by a WCDMA receiver (sensitivity) is -107 to $-104dBm$. In particular, the sensitivity test for such a receiver must be done in presence of the transmitter leakage. Thus, the sensitivity test requires the receiver to detect such an input signal with the desired SNR in the two following scenarios:

- A $3.84MHz$ bandwidth modulated signal at a $45MHz$ offset frequency (or greater, up to $190MHz$), generating a second order distortion around DC frequency
- A $3.84MHz$ bandwidth modulated signal at a $45MHz$ offset frequency, together with a modulated signal at a $20MHz$ with an input power of $-46dBm$, generating a third order distortion around DC frequency.

Noise Figure

The noise figure (NF) of the UTRA receiver is calculated from the standard's reference sensitivity test. The desired channel power is $P_R = 107dBm$. Using the previously determined $(E_b/N_t)_{eff}$ requirement and including the user data processing gain, the maximum allowable noise power within the channel bandwidth is calculated to be

$$P_{N,acceptable} = P_R - \left(\frac{E_b}{N_t}\right)_{eff} + G_P = -107dBm - 17dBm + 25dB = -99dBm \tag{4.11}$$

When the NF of the receiver and the bandwidth (B) are known, the actual noise power is determined using

$$P_{N,actual} = NF + 10Log_{10}(kTB) = NF - 108dBm \tag{4.12}$$

Since the actual noise power must be lower than or equal to the acceptable noise power, the NF requirement is

$$NF \leq P_{acceptable} + 108dBm = -99dBm + 108dBm = 9dB \tag{4.13}$$

This NF requirement is for the entire receiver. Subtracting the loss of $4dB$ in the duplex circuit, the NF requirement for the rest of the receiver is $5dB$. This level appears to be within reach for low cost integrated receivers. It should be noted that the NF must be met in the presence of the transmitter leakage signal, such as the sensitivity test.

Adjacent Channel

In 3G WCDMA standard the first adjacent channel is a $3.84MHz$ bandwidth modulated signal, located just close to the desired input signal. In this test, the desired signal power is $P_R = -93dBm$. Since this level is $14dB$ above the sensitivity limit, noise is of minor importance. The first adjacent channel has a power of $P_{AC1} = -52dBm$ ($41dB$ higher than the desired signal), centered around a $5MHz$ offset. Furthermore, this test requires that the receiver is able to detect an input signal with an input power varying from $-93dBm$ to $-66dBm$, with an adjacent channel input power $41dB$ higher (i.e. up to $-25dBm$).

The adjacent channel, due to its particular relative position with respect to the desired signal, is responsible either of a second order distortion and of a third order distortion in the channel bandwidth, thus both of this issues must be taken in account. Moreover, this test can be also critical for the receiver saturation, because the adjacent channel is a very high level blocker and it is very close to the desired channel frequency, so that it is difficult to filter it out.

GSM Blocker Test

This test requires that the receiver is able to detect the input signal in presence of a GMSK modulated narrowband interfering signal, with the desired SNR. The test scenario requires an input signal at f_0 frequency with a $-95dBm$ input power, and a GMSK modulated signal at frequency $|f - f_0| = 2.7MHz$, with a $-57dBm$ input power

The influence of this test could be important to set the tolerable signal swing for all the single blocks of a receiver, because this blocker can saturate the circuits and thus they can reduce the receiver performances.

Intermodulation Tests

Third order distortion mechanisms, due to the presence of two interfering signals, can produce a further interfering signal in the band of the desired channel. The 3G WCDMA standard requires that the receiver is capable to detect

the wanted signal in the presence of two interfering signals which have a specific frequency relationship with the wanted signal itself. In particular the standard requires that the receiver must detect the wanted signal with the desired SNR in the following two cases:

1. The wanted signal is $3dB$ greater than the sensitivity (i.e. $P_R = -104dBm$), and the two interfering signals are offset 10 and $20MHz$ from the desired signal. The first interferer is a CW signal at $P_I = -46dBm$, while the second one is a modulated signal with a power of $P_I = -46dBm$.

2. The wanted signal is $10dB$ greater than the sensitivity (i.e. $P_R = -97dBm$), and the two interfering signals are offset 3.5 and $5.9MHz$ from the desired signal. The first interferer is a CW signal at $P_I = -44dBm$, while the second one is a GMSK modulated signal with a power of $P_I = -44dBm$.

Especially in the first case, where the desired signal is very close to the minimum sensitivity, both noise and interference must be taken into account, also when the respective $IIP3$ is computed. For example, for the first test, the maximum level of noise and interference is found to be

$$P_{N+I}(10/20MHz) = P_R - \left(\frac{E_b}{N_t}\right)_{eff} + G_P = -96dBm \tag{4.14}$$

where P_{N+I} is referred to antenna input. In this test case, several interfering products are created, thus the allowable noise and interference power P_{N+I} must be distributed. The power level corresponding to each of the interfering or blocking products can be estimated (taking account of a reasonable implementation margin) as $P_{N+I} - 8dB = -104dBm$. This power level, along with the relationship between intermodulation power level and input intercept point, gives the minimum receiver $IIP3$:

$$IIP3(10/20MHz) \geq P_I + \frac{1}{2}(P_I - (P_{N+I} - 8dB)) = -17dBm \tag{4.15}$$

Similarly, it is possible to compute the maximum level of noise and interference and the minimum $IIP3$ for the second test:

$$P_{N+I}(3.5/5.9MHz) = P_R - \left(\frac{E_b}{N_t}\right)_{eff} + G_P = -89dBm \tag{4.16}$$

$$IIP3(3.5/5.9MHz) \geq P_I + \frac{1}{2}(P_I - (P_{N+I} - 8dB)) = -20.5dBm \tag{4.17}$$

4.2 Front-End Overview

The block diagram of the Front-End described in this chapter is pictured in Fig. 4.2. The Front-End is built by the following blocks:

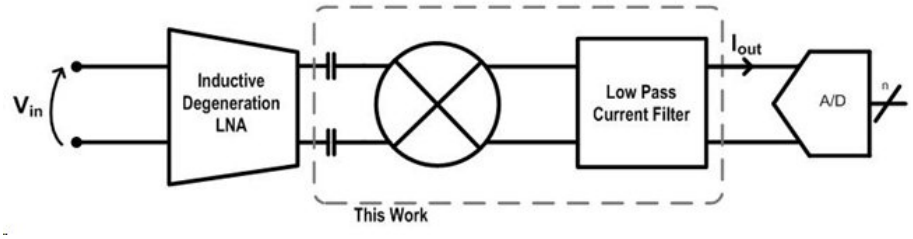

Figure 4.2: Front-End Block Diagram

- an inductive degeneration LNA, with a current as the output signal
- a current-mode passive mixer
- a current-mode channel selection filter, with a virtual ground at the input
- an analog-to-digital converter with a current as the input signal ([24])

The main peculiarity of this front-end is the current-mode design for all the receiver blocks. In fact the input voltage is immediately converted in a current signal by the LNA transconductor, and it remains a current along the whole receiver path. This allows to have both the current-mode passive mixers and the "pipe filters" advantages, as it will be explained deeply in the following sections.

The inductive degeneration LNA is not part of this job: thus, to design and simulate the front-end an ideal but noisy LNA has been used. In particular, an LNA with the followig performances has been considered:

- $35mS$ of single-ended transconductance
- $1.2k\Omega$ of output resistance and $150fF$ of output capacitance (including the layout parasitc capacitance)
- $1.7dB$ of Noise Figure with a 200ω of resistive load

The work described in this chapter is focused on the design of the downconversion/baseband blocks of the front-end. In particular, a "pipe filter" (see section 2.3) has been used as the channel selection filter.

The simulation reported in this chapter has been done using a 65nm CMOS technology.

4.3 Current-Mode Passive Mixers for Downconversion

4.3.1 Introduction to Current-Mode Passive Mixers

Contrary to standard active mixers (like the Gilbert Cell, [25]), in a passive mixer ([26]) the bias current is totally absent, thus all the mixer transistors are in the linear region, i.e. they work as switches and they don't have any power consumption at DC frquency. This lack of bias current means also that no flicker noise is present at the output, at least in ideal cases.

The current-mode passive mixer is pictured in figure 4.3. This structure works

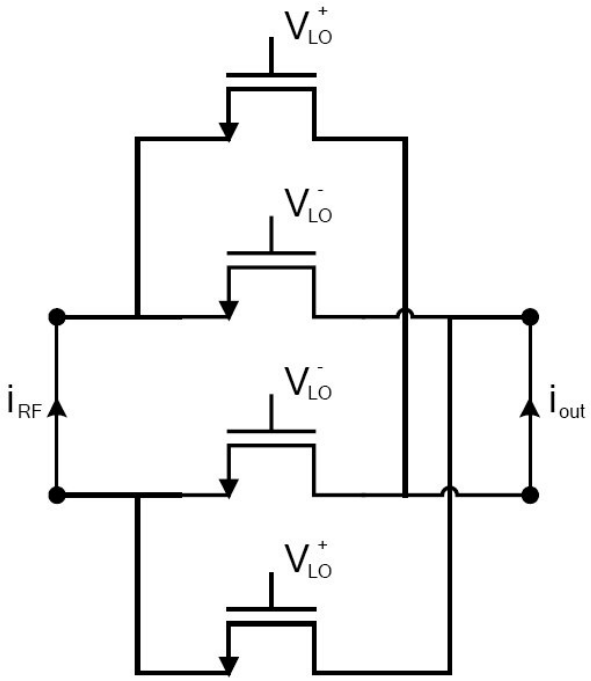

Figure 4.3: Current-Mode Passive Mixer

only with current signals and operates a frequency translation based on the local oscillator V_{LO}. Therefore, if the passive mixer is used in a receiver chain, the previous stage has to provide an RF current signal (such as a transconductor) and the following stage has to manage a baseband input current (such as a current filter or a virtual ground). The transconductor can be similar to the classical one used for the GIlbert Cell, with just one important difference: in this case the transconductor bias current is uncorrelated to the switching pairs design, because they don't have any bias current. The main requirement for a current-mode passive

mixer load on the contrary is a low input impedance at the desired frequencies, because it has to manage current signals.

The current-mode passive mixer cannot provide a current gain itself, but an overall gain G can be achieved thanks to the transconductor and to the load stages:

$$G = G_{m,RF} \cdot \eta_c \cdot R_{load} \tag{4.18}$$

where $G_{m,RF}$ is the transconductance gain of the previous stage, η_c is the passive mixer conversion efficiency and R_{load} is the load transimpedance gain.

The η_c factor deserves a further discussion because it depends on several design parameters. In current-mode mixer topology the switching pairs source voltage is super-imposed by other stages bias. In particular, in most of cases it is set by the load bias, because the passive mixer is often AC coupled with the previous stage. Therefore, the choice of the local oscillator bias voltage sets the operating point of the switching pairs. In order to analyze this circuit, the switching pairs can

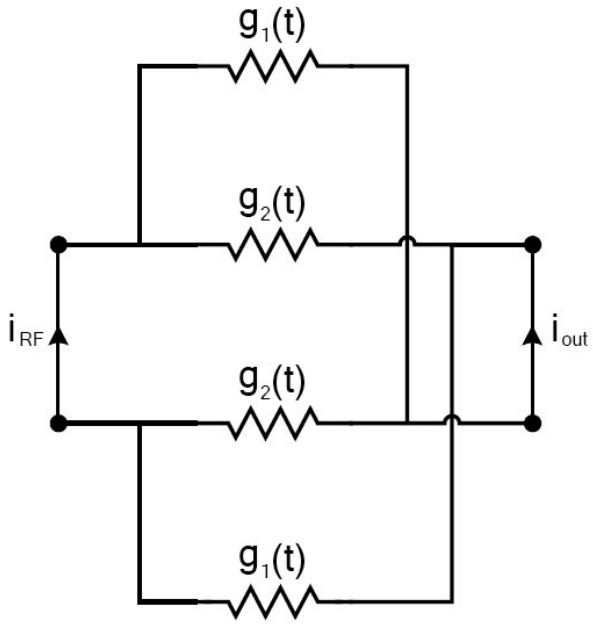

Figure 4.4: Current-Mode Passive Mixer: Small Signal Model

be considered as periodic time-variant conductances, with the same period of the local oscillator T_{LO}. The small signal equivalent circuit is pictured in Fig. 4.4, where $g_1(t) = g_{ds}(t)$ and $g_2(t) = g_{ds}(t - \frac{T_{LO}}{2})$ and $g_{ds}(t)$ is the MOS time-variant channel conductance. Thus, the device conductance in each pair results in opposite phase. Assuming an infinite output impedance for the driving stage and

a zero impedance for the load, the signal output current results:

$$i_{out} = \frac{g_{ds}(t) - g_{ds}(t - \frac{T_{LO}}{2})}{g_{ds}(t) + g_{ds}(t - \frac{T_{LO}}{2})} i_{RF}. \tag{4.19}$$

An ideal switching behavior for the pairs is assumed (i.e. $g_{ds} = \infty$ when the switch is ON and $g_{ds} = 0$ when the switch is OFF). By choosing a local oscillator bias voltage equal to the MOS switching voltage V_{sw}, in both pairs a device turns on at the same moment when the other device turns off. This corresponds to the ideal 50% Duty Cycle. Since the conversion efficency in a mixer is equal to the first term of the transfer function Fourier serie ([26]), in this case it is equal to

$$\eta_c = \frac{2}{\pi} \tag{4.20}$$

More than the 50% Duty Cycle case there are 2 further oscillator bias voltage configurations. If the local oscillator bias voltage is greater than V_{sw} there would be an on-overlap time range Δt with both MOS turned on; on the contrary, if the local oscillator bias voltage is lower than V_{sw} there would be an off-overlap time range Δt with both MOS turned off. In these cases, the (4.20) changes versus the overlap time range. Since the simultaneous turning on of both MOS creates an output common mode voltage, it is possible to make an unique discussion considering both MOS turned off for a time range Δt. Thus, it can be proved that the conversion efficiency becomes

$$\eta_c = \frac{2}{\pi} \cos(\pi \frac{\Delta t}{T}). \tag{4.21}$$

It can be noticed that for small Δt the variations can be negligible with respect to the ideal configuration.

If real MOS model is considered as switching pair, this issue can get more complicated. In fact, the MOS don't have just two different working region, therefore it is necessary to compare the MOS channel impedance with the driving output impedance. The assumptions made in the previous paragraphs make sense only if the g_{ds} time mean value is less lower than the output driving impedance and if the load input impedance is negligible. The MOS conductance is

$$g_{ds} = K \frac{W}{L} (V_{GS} - V_{th}) \tag{4.22}$$

for $V_{GS} > V_{th}$, where W, L are the MOS sizes, V_{th} is the MOS threshold voltage, V_{GS} is the gate-source voltage and K is a tecnology dependent parameter. In general the time mean g_{ds} increases with V_{GS} (i.e. with bigger local oscillator amplitude) or with the channel width W. However a W increase has a significant drawback, because it increases also parasitic capacitances.

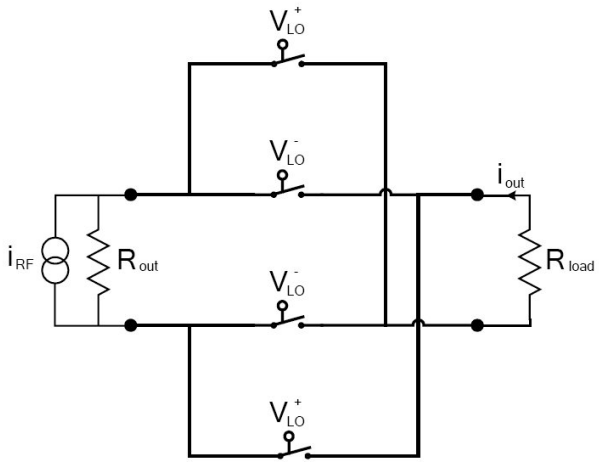

Figure 4.5: Current-Mode Passive Mixer with finite Driving Impedance and Load

Finally, it is considered the circuit reported in Fig. 4.5, where the transistors are replaced by ideal switches but the load is not a short-circuit and the driving output impedance is not infinite. In this case the conversion efficiency becomes

$$\eta_c = \frac{2}{\pi}\frac{R_{out}}{R_{load+R_{out}}}\cos\left(\pi\frac{\Delta t}{T}\right) \tag{4.23}$$

which is the same expression of (4.21) with a further attenuation term, depending on R_{load} and R_{out}. Thus it can be notice that it is necessary to keep $R_{load} \ll R_{out}$ in order to not deteriorate the conversion efficiency. As a consequence, it is also necessary that the switch impedance is kept much lower than R_{out}, because it results in series with the load impedance.

4.3.2 Current-Mode Passive Mixer Design

The passive mixer structure implemented for the front-end in point, is reported in Fig. 4.6. It is an NMOS current-mode passive mixer, with an AC coupling behind it. Thus the source voltage of the switching pairs is decided by the baseband filter bias.

The current-mode passive mixer design parameters are the following:

- $C_c = 2pF$. The AC coupling capacitances have been chosen large enough to have a series RF impedance, negligible compared to the load impedance (virtual ground plus switching pairs), in order to avoid an undesirable voltage swing at LNA output. Moreover, this capacitances have to be kept as little as possible in order to minimize the active area and to minimize the parasitic capacitance that could decrease the LNA output impedance.

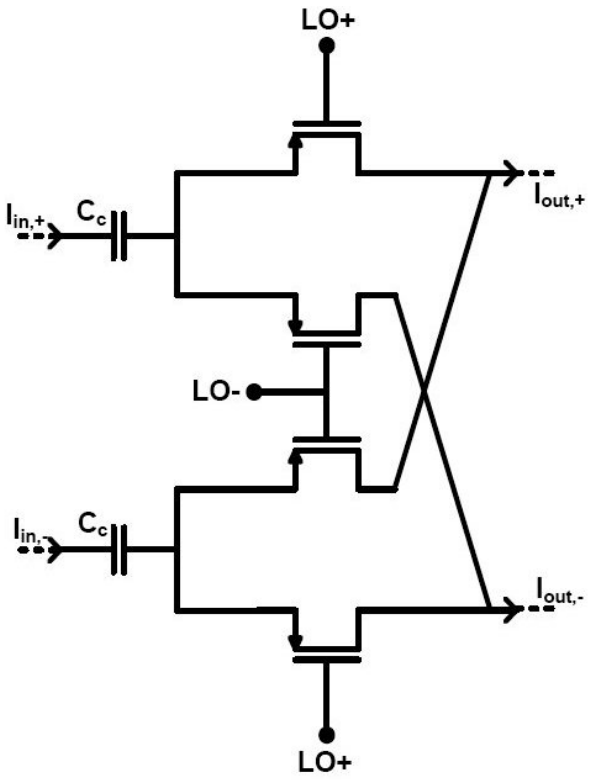

Figure 4.6: Passive Mixer Structure

- $A_{LO} = 1.2$. The local oscillator is an ideal square wave with finite rise time and fall time. Its amplitude has been designed as large as possible in order to maximize the switching pair linearity

- $V_{gs} = 650mV$. The LO voltage mean value has been chosen in order to have the best trade off in terms of conversion efficiency and linearity

- $W/L = 20\mu m/60nm$. The transistor size has been chosen in order to have the best trade off in terms of noise and linearity. In fact a little MOS width has little parasitic capacitance but leads to big channel resistance, on the contrary a big MOS width has little channel resistance with big parasitic capacitance. Moreover, the minimum channel lenght is a mandatory choice because it is the best solution both in terms of channel resistance and parasitic capacitance

4.4 Alternative "Pipe Filter" Biquad Cell

In this section, an alternative "pipe" biquad cell (besides the one described in section 3.1) is presented.

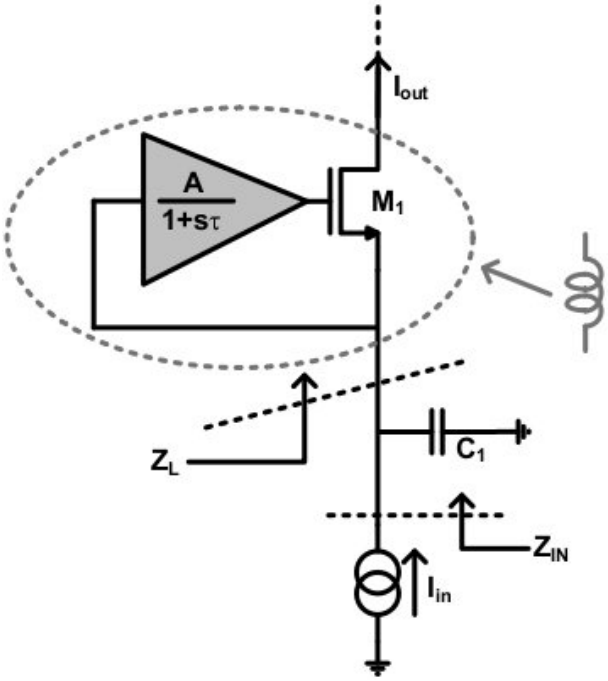

Figure 4.7: Alternative Current Biquad Cell

Also this current biquad cell, reported in Fig. 4.7, implements an active inductor, realized through the network formed by transistor M1 and an inverting gain stage with a real pole located at $\frac{1}{\tau}$. At DC frequency, the gain stage boosts the M1 transconductance and reduces the active inductor input impedance Z_L by a $(1 + A)$ factor. When frequency increases, the gain decreases until the M1 gate small signal voltage gets to zero and the input impedance becomes $Z_L = 1/g_m$. In particular, the active inductor input impedance is equal to:

$$Z_L(s) = \frac{1 + s\tau}{g_m[(1 + A) + s\tau]} \tag{4.24}$$

The (4.24) is equivalent to an inductance $L = \frac{\tau}{g_m A}$ together with a series resistance $R_S = \frac{1}{Ag_m}$ and a shunt resistance $R_P = \frac{1}{g_m}$.

This active inductor, together with the $C1$ capacitance, is an active RLC network that can synthetize a couple of complex conjugated poles. This is a current

mode biquad cell with the following transfer function:

$$\frac{I_{out}}{I_{in}}(s) = \frac{g_m[(1+A)+s\tau]}{g_m(1+A)+s(C1+g_m\tau)+s^2C1\tau} \tag{4.25}$$

The cell has an in-band current gain equal to 1, therefore is a loseless pipe with the same properties as the current biquad cell described in chapter 3. The frequency of conjugated poles ω_0 and their quality factor Q are given by

$$\begin{cases} \omega_= & \sqrt{\frac{(1+A)g_m}{C1\tau}} \\ Q = & \frac{\sqrt{C1\tau g_m(1+A)}}{C1+g_m\tau} \end{cases} \tag{4.26}$$

In this case, the biquad cut-off frequency ω_0 depends on the transistor transconductance g_m multiplied by the gain boost $(1+A)$, on the capacitance $C1$ and on the gain stage real pole $\frac{1}{\tau}$.

While the filter transfer function has a low-pass shape, the input impedance of the filter corresponds to that of a LCR shunt resonator and is given by

$$Z_{in}(s) = \frac{1+s\tau}{g_m(1+A)+s(C1+g_m\tau)+s^2C1\tau} \tag{4.27}$$

The band pass shape of the input impedance gives a low impedance ($\frac{1}{Ag_m}$) close to DC (due to the presence of the gain boost) and it goes to zero at extremely high frequencies (due to the capacitance C1).

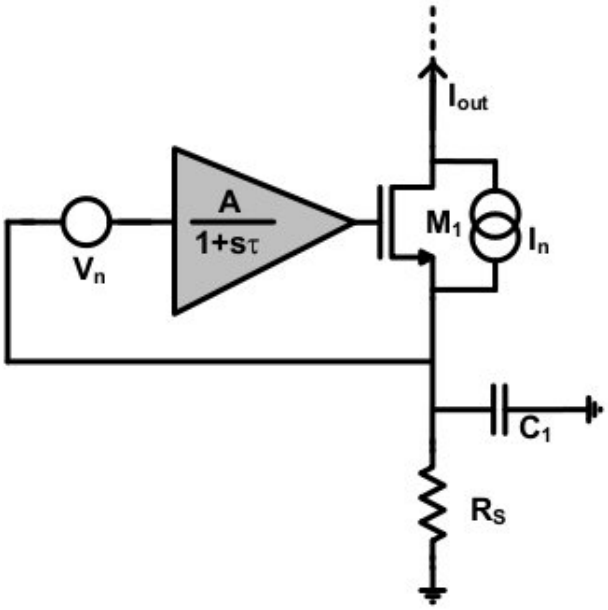

Figure 4.8: Biquad Noise Sources

In Fig. 4.8 are reported the two noise sources of this current biquad cell, the M1 transistor and the gain stage. In particular the gain stage noise, is represented as a noise voltage generator V_n at the input of the stage itself. This is because it is not important to evaluate the absolute value of the output noise at this moment, but it is very interesting to analyze the frequency behavior of the noise itself.

Under the assumption of white noise sources and a finite driving resistance $A \gg 1$ and $g_m R_s \gg 1$, the transfer functions from the noise sources associated to transistor M1 and to the gain stage to the output are given by:

$$\frac{I_{out}}{I_n}(s) \approx \frac{(1 + C1R_s s)(1 + s\tau)}{s^2 C1R_s + s(C1R_s + g_m R_s \tau) + A g_m R_s} \tag{4.28}$$

$$\frac{I_{out}}{V_n}(s) \approx \frac{A g_m (1 + C1R_s s)}{s^2 C1R_s + s(C1R_s + g_m R_s \tau) + A g_m R_s} \tag{4.29}$$

These noise transfer functions have both a high-pass shape, thus they confirm that this biquad cell has the "pipe filter" noise properties, i.e. its in-band noise spectral density is low, compared to classical voltage filters, and it is uncorrelated to the pole frequency ω_0. In particular, while the M1 noise transfer function has two poles and two zeros and thus it has an actual high-pass shape, the gain stage noise transfer function has just one zero and thus it has an actual band-pass shape. This is because this noise is filtered out by the gain stage real pole.

The biquad cell presented here has also a big advantage in terms of linearity, with respect to the biquad cell described in chapter 3. In fact, in the previous case, the current flowing in the first non-linear element (M1 in Fig.3.1) is low-pass filtered with a first order transfer function, because the second order filtering action is performed also by the $C2$ capacitance, located after M1 in the current path. On the contrary, in this case the whole second order filtering action is performed before the only non-linear element M1, thanks to the presence of the transistor g_m boost. This fact has a very important implication for a channel selection filter used in a receiver front-end: the out-of-band blockers can be filtered out with a higher order selectivity before entering the non-linear devices and thus before perturbing the desired signal. This is the reason why this version of "pipe" biquad cell is better than the prevoius one in terms of out-of-band linearity.

4.5 Baseband Filter Implementation

To ensure enough out-of-band filtering, the baseband filter has been designed as a 3^{rd} order filter with a current biquad cell (Section 4.4) cascaded with a single real pole. In Fig. 4.9 it is shown the actual channel filter implementation.

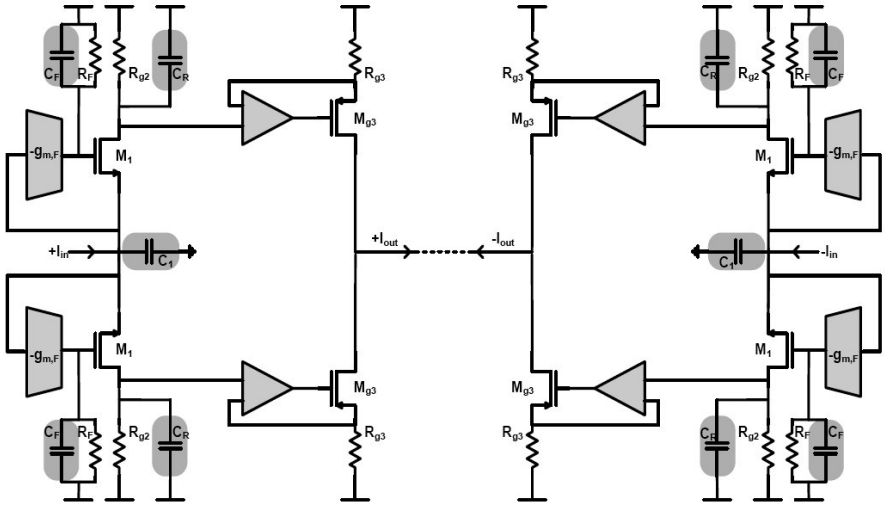

Figure 4.9: Whole Filter Overview

The filter has been implemented in a folded P-N version, in order tho have an equivalent input transconductance two times bigger than the single NMOS g_m, with the same current consumption. This means that a two times lower input impedance can be synthetized. This is a very important issue because this filter has to be used also as a virtual ground that loads a current mode passive mixer, thus the linearity can be improved without any cost in terms of power consumption.

The feedforward gain filtering stage has been implemented with a transconductance $g_{m,F}$ stage loaded with a shunt RC network that defines both the gain and the stage pole. In fact, the following parameters defined in Section 4.4 can be rewritten as:

$$\begin{cases} A = & g_{m,F} \cdot R_F \\ \tau = & \frac{1}{C_F R_F} \end{cases} \tag{4.30}$$

The current mirror configuration reported in Fig. 4.9 has been implemented in order to maximize the mirror linearity performances. This is because the $M1$ drain is an high impedance node, where the voltage swing is relatively high. In this case this voltage swing is ideally linear because it is determined just by the mirror resistance R_{g2}. Furthermore this voltage swing is exactly reported at the M3 sources thanks to the virtual short of the operational amplifier input. If $R_{g2} = R_{g3}$ the M_{g3} drain current will be equal to the $M1$ drain current, with a distortion inversely proportional to the virtual short strenght.

The C_R capacitance implements, together with the R_{g2} resistance, the real poles, that is necessary to sinthetize the third order function.

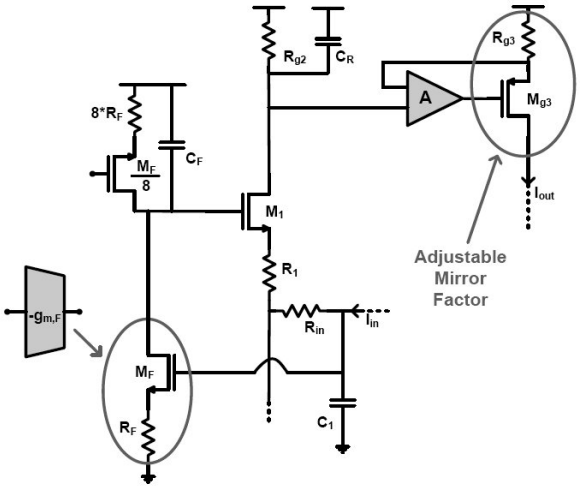

Figure 4.10: Filter Schematic Detail

In Fig. 4.10 is reported the actual schematic of the channel selection filter. For the sake of simplicity is reported just the upper side of a single branch.

At the filter input a R_{in} resistance is used to modify the complex conjugated poles frequency, in order to be able to synthetize the same cut-off frequency with a capacitance value that is significantly lower. This resistance doesn't have any DC voltage drop and doesn't affect the bias configuration but it has a drawback, in fact this resistance increase the filter input resistance. In order to reduce this effect, the R_{in} resistance is inserted inside the feedforward loop, and thus it is also reduced by a factor $(1 + A)$.

In order to improve the filter linearity, every transistor has been degenerated with a linear resistance, whose value is approximately the inverse of the relative transistor transconductance.

In order to have a feedforward gain as accurate as possible, the stage load has been implemented with a degenerated transistor 8 times more little than the transconductor M_F: the matching between the two transistors is thus able to assure enough gain precision.

Through the size variation of the M_{g3} transistor and the R_{g3} resistor it is possible to adjust the current mirror factor and thus to implement a signal gain variation in this point of the receiver path.

4.6 Baseband Filter Design

The baseband filter has been designed to work both for a GSM and for a UMTS configuration. The biquad cell can be tuned by changing the input resistance R_{in} and the OTA load capacitance C_F, while the real pole can be tuned by changing the capacitance C_R. The OTAs are implemented in a fully differential version, one for each side of the filter (NMOS and POMOS). The DC voltage headroom has been set to $V_{dd} = 2.5V$.

The baseband filter design parameters are the following:

- The biquad cell bias current I_{bias} has been set to $50\mu A$ per branch. This is the minimum current that is able to manage all the high level blockers without desensitizing the desired input signal.

- The OTA power consumption is $550\mu A$ for each side. This is a trade-off between the OTA in-band noise and the power consumption itself. It can be noticed that the OTA output noise transfer function has a high-pass shape component whose noise spectral density is linearly proportional to the transconductance $g_{m,F}$.

- Each current mirror opamp has a $20\mu A$ power consumption. Also in this case it is a trade-off between output noise and power consumption. In particular, to evaluate the output noise, the input opamp transconductance has to be compared with the transistor $M_{g,3}$ output resistance.

- The OTA gain has ben set to 8. This gain has to be high enough to assure a low input impedance, but it has to be enough accurate in order to set the poles position without degrading the circuit Error Vector Magnitude (EVM). The more this gain becomes high, the more critical becames the poles position accuracy, because of the parasitic effect of the M_F transistor output impedance

- The $M_{g,2} - M_{g,3}$ mirror factor has been set to 2 in the UMTS configuration, while it has been set to 1 in the GSM one. This is because the UMTS noise requirements are more strict and the higher current gain can reduce the input referred noise of the $M_{g,3}$ transistor and of the $R_{g,3}$ resistance.

- The poles position is the main difference between the UMTS filter configuration and the GSM one. In particular, in the UMTS filter version the biquad complex conjugated poles frequency has been set to $4MHz$ with a Q factor of 1 and the real pole frequency has been set to $3MHz$, while in the GSM

filter version the biquad poles frequency has been set to $1MHz$ and the real pole frequency has been set to $200kHz$. This frequency values have been chosen in order to assure enough selectivity to manage the high level near blockers by filtering them out before entering the non-linear devices

- The resulting total capacitance is $140pF$ single-ended plus $120pF$ differential for the UMTS configuration and $140pF$ single-ended plus $210pF$ differential for the GSM one.

- The total baseband filter current consumption is $1.48mA$ for the UMTS version and $1.38mA$ for the GSM one. This difference is due to the different current mirror factor of the filter itself.

4.7 Front-End Simulation Performances

In this section the simulated Front-End performances are reported for the 3 working configurations.

4.7.1 UMTS configuration

In this configuration the front-end shows an in-band transconductance gain between the LNA voltage input and the filter current output of $-32.5dB$. The Delta Gain between the bandwidth edge frequency ($2MHz$) and the in-band value is $-0.7dB$ and the overall noise figure is $1.86dB$.

In Table 4.3 are reported the linearity test results. In particular the P_{out}, $IM2$, $IM3$ are calculated assuming a 1 Ohm resistance at the filter output: the P_{out} column is the output desired signal while $IM2$ and $IM3$ are the 2^{nd} and 3^{rd} order intermodulation distortions. It can be noticed that all the linearity tests can

Test	P_{in}	P_{out}	IM2	IM3
$-22dBm$@$45MHz$	REFSENS ($-110dBm$)	$-143dBm$	$-155dBm$ IIP2:$66dBm$	$-200dBm$
$-28dBm$@$5MHz$	$-72dBm$	$-105dBm$	$-142dBm$	$-110dBm$ IIP3:$-3.3dBm$
$3.5MHz/5.9MHz$	REFSENS $+10dBm$	$-133dBm$	–	$-158dBm$
$10MHz/20MHz$	REFSENS $+3dBm$	$-140dBm$	–	$-207dBm$

Table 4.3: Front-End Performances - UMTS Configuration

be succesfully passed by the front-end UMTS configuration.

4.7.2 GSM 900MHz configuration

In this configuration the front-end shows an in-band transconductance gain between the LNA voltage input and the filter current output of $-40dB$. The Delta Gain between the bandwidth edge frequency ($100kHz$) and the in-band value is $-0.9dB$ and the overall noise figure is $1.55dB$.

In Table 4.4 are reported the linearity test results. It can be noticed that all the

Test	P_{in}	P_{out}	IM2	IM3
$-73dBm@200kHz$	$-82dBm$	$-125dBm$	$-228dBm$	$-229dBm$
$-41dBm@400kHz$	$-82dBm$	$-125dBm$	$-157dBm$	–
	Gain Compression: $0.25dB$			
$800kHz/1.6MHz$	$-99dBm$	$-142dBm$	–	$-155dBm$
$-46dBm@6MHz$	$-99dBm$	$-142dBm$	$-214dBm$	–
$-23dBm@3MHz$	Gain Compression: $0.15dB$			

Table 4.4: Front-End Performances - GSM $900MHz$ Configuration

linearity tests can be succesfully passed by the front-end GSM $900MHz$ configuration.

4.7.3 GSM 1800MHz configuration

In this configuration the front-end shows an in-band transconductance gain between the LNA voltage input and the filter current output of $-41.5dB$. The Delta Gain between the bandwidth edge frequency ($100kHz$) and the in-band value is $-0.9dB$ and the overall noise figure is $1.95dB$.

In Table 4.5 are reported the linearity test results. It can be noticed that all the linearity tests can be succesfully passed by the front-end GSM $1800MHz$ configuration.

4.8 Conclusions

In this chapter the receiver specifications for both GSM and UMTS standards have been derived. Furthermore a current-based reconfigurable front-end has been described, with particular focus to the channel selection filter block. For this purpose, a "pipe filter" biquad cell has been used.

Test	P_{in}	P_{out}	IM2	IM3
$-73dBm@200kHz$	$-82dBm$	$-127dBm$	$-231dBm$	$-235dBm$
$-41dBm@400kHz$	$-82dBm$	$-127dBm$	$-166dBm$	–
	Gain Compression: $0.2dB$			
$800kHz/1.6MHz$	$-99dBm$	$-144dBm$	–	$-160dBm$
$-46dBm@6MHz$	$-99dBm$	$-142dBm$	$-207dBm$	–
$-23dBm@3MHz$	Gain Compression: $0.1dB$			

Table 4.5: Front-End Performances - GSM $1800MHz$ Configuration

This "pipe filter" topology presented is quite different with respect to the one described in chapter 3 and it has a significant advantage: the input current signal that enter the non-linear device is filtered out by a second order filtering function. This is a very large improvement for the filter linearity, in particular in the interferers scenarios where high level blockers are located out of the filter band.

The simulation results of the front-end totally fit with the GSM and UMTS specs derived in the first section.

Conclusions

In this thesis, a new class of filters based on the concept of "pipe filtering" was presented.

The work starts from an overview of the channel selection filters state-of-the-art, with particular attention to the most effective techniques used to maximize the filter spurious free dynamic range.

After this introduction, the standard filters $\frac{kT}{C}$ limit has been analyzed in terms of total integrated noise and of frequency behavior. The core of this limit is actually the output signal sensing as a voltage across the filtering capacitor. Therefore, a different solution has been proposed: the output signal can be sensed as a current, for example the current flowing out from the resistance in a 1^{st} order RC filter. This results in a high pass output noise transfer function and consequentially in an in-band signal-to-noise ratio increase. In particular, in a 1^{st} order RC filter, the SNR improvement is $5.6dB$ in favor of the current mode: it means that a current filter can have the same in-band noise than a voltage filter with 4 times less capacitance area. Furthermore, the "pipe filter" concept has been introduced to indicate this class of current filters that behave as a loseless pipe in the filter band, when the output current is exactly equal to the input current and no noise or distortion can be introduced.

The first and the most simple real implementation of a "pipe filter" is a single-pole cell built by a common gate stage and a single capacitance. This cell validates the whole "pipe filter" theory in terms of noise and linearity performance, but it has some drawbacks. In particular it has an input impedance relatively high and it cannot synthetize complex conjugated poles. For this purpose, a "pipe filter" biquad cell with an in-band zero input impedance has been presented and analyzed. Furthermore an integrated CMOS $90nm$ "pipe filter" prototype has been realized. It is a 4^{th} order Butterworth filter, designed for WCDMA standard. The experimental results confirm the "pipe filter" theory: in fact, the filter prototype shows a $1.26mW$ power consumption, the lowest of the state-of-the-art, with a total filtering capacitance of $210pF$. Besides, the filter shows a $75dB$ SFDR, and a figure of merit ([1]) $6dB$ higher that the the state-of-the-art.

In the last part of this thesis, a totally current-based receiver front-end has

been described. It is a multistandard reconfigurable front-end for both GSM and UMTS. After a GSM and UMTS general features overview and a brief specs derivation for both standards, the front-end design has been shown in detail. In particular an alternative "pipe filter" biquad cell, more suitable for a current-based receiver, has been presented and analyzed. The front-end has been simulated with a $65nm$ technology, using an ideal LNA, to verify the performances of the pipe filter when it is used as a passive mixer load. The noise figure of the front-end is between $1.55dB$ for the GSM $900MHz$ configuration and $1.95dB$ for the GSM $1800MHz$ configuration. Furthermore all the linearity tests for both standards have been passed succesfully by the designed front-end.

Bibliography

[1] A. Yoshizawa and Y. P. Tsividis, "Antiblocker design techniques for MOSFET-C filters for direct-conversion receivers", IEEE J. Solid-State Circuits, vol. 37, pp. 357-364, Mar. 2002

[2] Castello and Gray. "Performance limitations in switched- capacitor filters", Circuits and Systems, IEEE Transactions on (1985) vol. 32 (9) pp. 865 -876

[3] S. D'Amico, V. Giannini, A. Baschirotto, "A 4th-order active Gm-RC reconfigurable (UMTS/WLAN) filter", IEEE J. Solid-State Circuits, July 2006

[4] M. Banu and Y. Tsividis, "An elliptic continuous-time CMOS filter with on-chip automatic tuning", IEEE J. Solid-State Circuits, vol. SC-20, pp. 1114-1121, Dec. 1985.

[5] A. Yoshizawa and Y. P. Tsividis , "A channel-select filter with agile blocker detection and adaptive power dissipation" , IEEE J. Solid-State Circuits, May 2007

[6] D. Chamla, A. Kaiser, A. Cathelin, and D. Belot, "A gm-C low-pass filter for zero-IF mobile applications with a very wide tuning range", IEEE J. Solid-State Circuits, vol. 40, no. 7, pp. 1143-1450, Jul. 2005.

[7] D. Chamla, A. Kaiser, A. Cathelin, D. Belot, "A switchable-order Gm-C baseband filter with wide digital tuning for configurable radio receivers", IEEE J. Solid-State Circuits (2007), pp. 1513-1521.

[8] R. L. Geiger and E. Sánchez-Sinencio, "Active-filter design using operational transconductance amplifiers: A tutorial", IEEE Circuits Devices Mag., vol. 1, no. 2, pp. 20-32, Mar. 1985.

[9] S. D'Amico, M. Conta, A. Baschirotto, "A 4.1-mW 10-MHz Fourth-Order Source-Follower-Based Continuous-Time Filter With 79-dB DR", IEEE J. Solid-State Circuits, vol. 41, no. 12, pp. 2713-2719

[10] T. Hollman, S. Lindfors, M. Lansirinne, J. Jussila, K. Halonen, "A 2.7-V CMOS Dual-Mode Baseband Filter for PDC and WCDMA",IEEE J. Solid-State Circuits, vol. 36, no. 7, pp.1148-1153

[11] R. Kolm, W. Yan, H. Zimmerman, "Current-Mode Filter in 65nm CMOS for a Software-Radio Application", Circuits and Systems, 2008. ISCAS 2008. IEEE International Symposium On, pp. 3130-3133

[12] A. Tekin, H. Elwan, K. Pedrotti, and N. Dogan, "Noise-Shaped Post-Mixer Blocker Filter for Integrated Receivers", International Conference on Microelectronics, Dubai, Dec. 2008

[13] A. Liscidini, A. Pirola, and R. Castello, "A 1.25mW 75dB-SFDR CT Filter with In-Band Noise Reduction", International Solid State Circuit Conference 2009, Digest of Technical Papers, pp. 336-337

[14] Nyquist, "Thermal Agitation of Electric H. Nyquist, Charge in Conductors." Phisical Review, 32, 1928, pp. 110-113

[15] A. Pirola, A. Liscidini, and R. Castello, "Current-Mode, WCDMA Channel Filter with In-band Noise Shaping", IEEE J. Solid-State Circuits, vol. 45, no. 9, pp. 1770-1780

[16] Donald D. Weiner, John F. Spina. "Sinusoidal analysis and modeling of weakly nonlinear circuits". Van Nostrand Reinhold Company, 1980.

[17] P. Wambacq, W. Sansen, "Distortion Analysis of Analog Integrated Circuits" Boston, MA: Kluwer, 1998.

[18] A. Antoniou, "Gyrator using operational amplifier", Electron. Lett., 1967, 3, pp. 350-352

[19] O.K. Jensen, T.E. Kolding, C.R. Iversen, S. Laursen, R.V. Reynisson, J.H. Mikkelsen, E. Pedersen, M.B. Jenner and T. Larsen, "RF Receiver Requirements for 3GWCDMA Mobile Equipment", Microwave Journal, Vol. 43, No. 2, pp. 22-46, 2000

[20] Valla, M. Montagna, G. Castello, R. Tonietto, R. Bietti, I., "A 72-mW CMOS 802.11a Direct Conversion Front-End With 3.5-dB NF and 200-kHz 1/f Noise Corner", Solid- State Circuits, April 2005, Volume: 40, Issue: 4, pp 970-977

[21] M. Maina, "Ricevitore GSM in tecnologia CMOS: confronto tra architetture integrate e progettazione di un front-end a conversione diretta", *Tesi di Laurea*, Anno 2003/2004, Università di Pavia

[22] B. Razavi, "RF Microelectronics". Prentice Hall PTR, 1998

[23] Third Generation Partnership Project (3GPP), "UE Radio Transmission and Reception (FDD)," Technical Specification 25.101, Vol. 8.1.0, 2007-12

[24] M. Sosio, "Convertitore Sigma-Delta in corrente con funzione di selezione di canale per applicazioni DVB-T", *Tesi di Laurea*, Anno 2008/2009, Università di Pavia

[25] B. Gilbert, "A precise four quadrant multiplier with subnanosecond response," IEEE J. Solid-State Circuits, pp. 365-373, Dec. 1968

[26] S. Borsotti, "Studio di Mixer Passivi Current Mode per Tecnologie Super Scalate", *Tesi di Laurea*, Anno 2005/2006, Università di Pavia